TECHNISCHE UNIVERSITÄT WIEN
Vienna University of Technology

D I P L O M A R B E I T

A resonant plasmonic structure for fluorescence spectroscopy

Ausgeführt am
Institut für Festkörperphysik
der Technischen Universität Wien
und am
Austrian Institute of Technology, Biosensor Technologies

unter der Anleitung von
Ao.Univ.Prof. Dipl.-Ing. Dr.techn. Christoph Eisenmenger-Sittner sowie
Dr. Jakub Dostalek

durch

Stefan FOSSATI

Hainburger Straße 22/9, A-1030 Wien

_____ _____

Datum Unterschrift (Student)

Abstract

The detection of trace amounts of chemical and biological compounds is of increasing importance in numerous fields including medical diagnostics, environmental monitoring and food safety. A well-established sensitive method for the readout of detection assays for numerous analytes is fluorescence spectroscopy which relies on the use of fluorescent dye labels. The combination of fluorescence spectroscopy with plasmonic nanostructures offers attractive means to locally amplify fluorescence intensity emitted by fluorophore labels and thus improve the sensitivity of fluorescence assays. This approach is based on the coupling of the dipole moment of the fluorescence dye with the strongly confined electromagnetic field that occurs upon the resonant excitation of surface plasmons. These optical waves originate from oscillations of charge density at the surface of metallic films and metallic nanoparticles which is accompanied by strong enhancement of the electromagnetic field intensity and local density of states. When applied to fluorescence assays, this interaction can be utilized to selectively increase the excitation strength and improve the collecting efficiency of fluorescence light emitted vial surface plasmons at the sensor surface. This thesis presents an analysis of a new design of a plasmonic structure for epifluorescence readout geometry that utilizes arrays of metallic nanoparticles arranged in a diffractive lattice. A structure supporting collective localized surface plasmons at wavelength that coincide with absorption and emission wavelengths of red and near infrared dyes is investigated. Numerical simulations are employed to study and optimize its geometry. Photo-nanoimprint lithography and thermal evaporation are employed to prepare the designed structure and atomic force microscopy and electron microscopy are employed to verify its morphology. Optical spectroscopy is used for the measurement of spectrum of supported plasmonic resonances and for future implementation to fluorescence biosensors applications.

Zusammenfassung

Der Nachweis von Spuren chemischer und biologischer Verbindungen ist in vielen Bereichen, wie etwa der medizinischen Diagnostik, Umweltüberwachung oder Ernährungssicherheit, von wachsender Bedeutung. Eine gut etablierte, sensitive Methode zur Durchführung solcher Tests ist die Fluoreszenzspektroskopie, eine Methode die auf dem Einsatz fluoreszierender Farbstoffe basiert. Die Sensitivität solcher Fluoreszenz-Assays kann durch die Kombination mit plasmonischen Nanostrukturen, welche die Fluoreszenz-intensität lokal verstärken, stark verbessert werden. Dabei koppelt das Dipolmoment des Fluoreszenzfarbstoffes mit dem stark auf die Oberfläche konzentrierten elektro-magnetischen Feld von resonant angeregten Oberflächenplasmonen. Diese optischen Wellen entstehen durch die Anregung von Schwingungen der Ladungsträgerdichte in metallischen Filmen und metallischen Nanopartikeln und gehen mit einer dramatischen Verstärkung der elektromagnetischen Feldstärke und Zustandsdichte einher. Angewandt auf Fluoreszenz-Assays kann diese Wechselwirkung verwendet werden um die Anregung des Farbstoffes selektiv zu verstärken und die Licht-Sammeleffizienz durch gerichtete Abstrahlung zu erhöhen. In dieser Arbeit wird eine neue plasmonische Struktur vorgestellt und analysiert, die auf metallischen Nanopartikeln, angeordnet als regelmäßiges optisches Gitter, basiert. Eine Struktur, die kollektive Oberflächenplasmonen-Resonanzen an den Absorptions- und Emissionswellenlängen von Fluoreszenzfarbstoffen und im roten und infraroten Teil des Spektrums erlaubtm, wird untersucht. Numerische Simulationen werden eingesetzt um die Geometrie zu planen und zu untersuchen. Die optimierte Struktur wird mit Photo-Nanoimprint Lithographie und einem Bedampfungsprozess erzeugt und Raster-Kraft-Mikroskopie sowie Elektronenmikroskopie werden eingesetzt um die Morphologie zu bestimmen. Die Bestimmung der spektralen Eigenschaften erfolgt durch optische Spektroskopie, wie auch die spätere Anwendung als fluoreszenzbasierter Biosensor auf optischen Verfahren basieren wird.

Table of content

1. Introduction

Rapid detection of very low concentrations of analytes is an important task in numerous fields ranging from the detection of pathogens in body liquids for early disease diagnosis, drug and doping control, environmental protection to the detection of impurities in industrial applications. Currently, highly trained staff is required to conduct the tests either manually or using large, expensive automated facilities, which are for this reason only performed by a few specialized laboratories. Shipping the samples is often times the most time consuming task of the process and often, special preparation is required to avoid degradation of the sample during transport. Diagnosis at the point of care would improve the time to diagnosis significantly and avoid the requirement of sample preservation, minimizing the risk of introducing additional variation by preservation steps. Fully integrated biochips with highly sensitive and reliable plasmonic biosensors, produced at an industrial scale at low cost, can provide a sensitive platform for affordable and easy to use devices. On-chip preprocessing makes the method accessible to a larger user base and reduces the variation introduced by manual preparation. Optical biosensors with plasmonic enhancement have been employed to study multiple biomarkers simultaneously in an array format [1], proving diagnostic information on multiple compounds in one processing step. Recently, plasmonic nanostructures enhancing fluorescence immunoassays have been proposed [2], [3] to combine high sensitivity with a simple and cheap reader geometry, deployable in a point of care device. For the practical application in biosensors, the nanostructures need to be compatible with established industrial-scale production methods. Here, a nanostructure prepared by nanoimprint lithography is studied, a method easily scalable by roll-to-roll processes [4].

1.1. Biosensors

The term biosensor refers to devices converting the presence of an analyte on a recognition surface to mostly electrical signals using a transducer. Selectivity for a target analyte is achieved by the functionalization of the surface with a recognition layer. Viable recognition elements are antibodies, enzymes, peptides and nucleic acids, binding specifically to a target analyte. In label-free detection, real time monitoring of the analyte binding process is used to study for example the binding

kinetics, but the sensitivity is limited by the properties of the analyte. Further sensitivity enhancement is achieved by the addition of a secondary recognition element, functionalized with a signal enhancing label, which binds specifically to the captured analytes.

The transducer measures the chemical binding and converts the information to a physical property, which is then quantified. A variety of transducers is available as shown in Fig. 1:

Chemical: For example in qualitative pregnancy tests: The presence of human chorionic gonadotropin (hCG) in female urine is detected by the binding of the analyte to a labeled antibody and the capture of this complex by a recognition antibody in a test area. The presence of the analyte is observed as a color change of the test area.

Electrochemical: Two modalities are available: In the amperometric approach a current is created by the selective oxidation or reduction of the analyte on the sensor electrodes. This method is typically used for glucose measurements in blood. In potentiometric measurements, the ionic binding of analytes to the sensor material changes the resistive properties of an electronic component.

Quartz crystal microbalance: A surface of a high Q factor piezoelectric oscillator is used as recognition interface. The shift of the resonance frequency by the additional mass of the bound analyte is the output signal.

Optical: A large variety of sensors has been developed based on the change of optical sensor properties associated with the analyte binding. The sensors rely on the change of refractive index (SPR, waveguide), absorption (spectroscopy) or emission (fluorescence spectroscopy) of light. Optical sensors may be designed

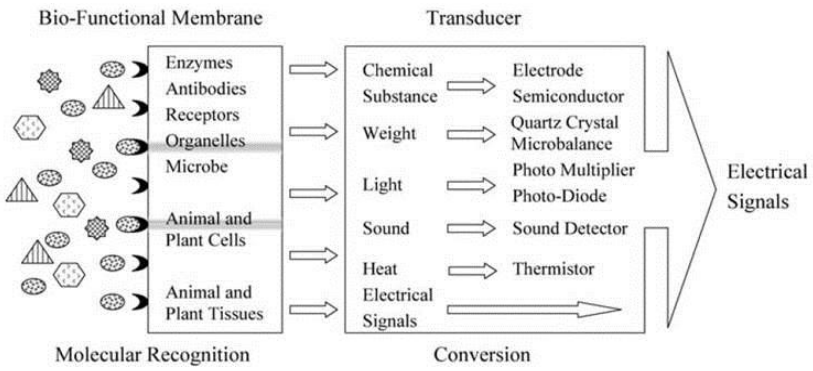

Fig. 1 Schematic of a biosensor [21]

with a functionalized recognition surface while others are used to probe assays solved in a bulk liquid or gas phase. In many cases, the signal can be enhanced by plasmonic effects.

1.2. Plasmonic biosensors

Plasmonic biosensors are photonic sensors, which employ the phenomenon of surface plasmon resonance (SPR) on metallic surfaces or metallic nanoparticles. The collective oscillation of the electron density, excited by light, confines the electromagnetic field within a few hundred nanometers in the dielectric and an order of tens of nanometers in the metal. Associated with the confinement is an increase in electromagnetic field intensity and high sensitivity to changes in the refractive index, which makes surface plasmons an excellent tool to probe assays on metallic surfaces. Besides the increased intensity at the surface, the background signal from compounds in the bulk medium is reduced by the exponential decay of the evanescent wave. Metallic nanoparticles of dimensions smaller than the wavelength support localized surface plasmon (LSP) modes with exceptional high enhancement of field intensities. These properties have been employed to significantly enhance well established optical methods by plasmonic effects, for example in surface enhanced Raman spectroscopy (SERS) [5], surface enhanced infrared spectroscopy (SEIRA) [6] and plasmon enhanced fluorescence spectroscopy (PEFS) [7], with great success. Especially for SERS, where the detection limit for Raman scattering has been pushed to the single molecule level [8]. The most widespread application nevertheless is PEFS due to the wide range of assays using fluorescent labeled probes.

1.3. Fluorescence spectroscopy

Chemical substances can transition to an excited electronic state by the absorption of a photon. The excited state is unstable and the molecule spontaneously relaxes into the ground state S_0 by a variety of relaxation processes. Radiative processes as well as no-radiative processes and combinations thereof exist and compete with each other. Phenomena including the emission of a photon are summarized under the term luminescence. Fig. 2 shows the Jablonski diagram of a fast (order of 10^{-8} s) relaxation process called

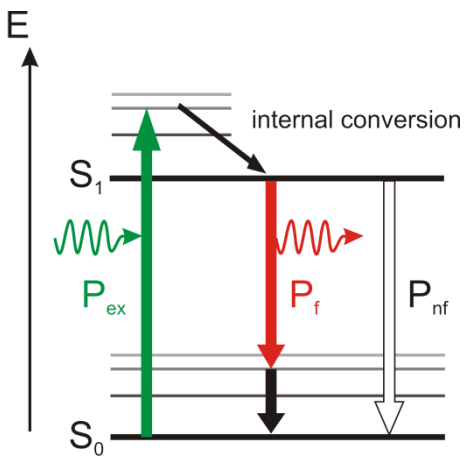

Fig. 2 Jablonski diagram of fluorescence

fluorescence typically found in aromatic molecules. In this process, the molecule is excited by the absorption of a photon from the ground state S_0 to an excited singlet state S_1. By photon absorption, the molecule is excited into a rotational and vibrational excited state with slightly higher energy then the respective electronic state. Within very short time (in the order of 10^{-15} sec), the molecule relaxes to the state S_1 by non-radiative internal conversion. For singlet states, the electron in the excited state S_1 is paired to the electron in the ground state S_0 by opposite spin, consequently the relaxation to the ground state by the emission of a photon is spin allowed and a fast. Similar to the excitation, the molecule does not relax to the ground state directly but to a vibrational excited state and returns to the ground state S_0 by internal conversion. Therefore, the energy of the emitted photon is smaller than the energy of the absorbed photon, the wavelength difference is denoted as Stokes shift. For a comprehensive overview on fluorescence please refer to [9].

The fluorescence emission shows dipole characteristics and competes with non-radiative processes, namely internal conversion, collisions and Förster resonance energy transfer. The fluorescence emission rate k_{em} depends on the fluorescent decay rate k_f and the non-fluorescent decay rate k_{nf} by

$$k_{em} = k_{ex}\frac{k_f}{k_f + k_{nf}}. \quad (1)$$

The excitation rate of the fluorophore is proportional to the second power of the local electric field $k_{ex} \sim E_0^2$.

Fluorophores

Chemical compounds capable of the re-emission of light upon excitation are called fluorophore and typically contain a number of coupled aromatic groups. Numerous polymers and biological molecules show autofluorescence when illuminated with light in the UV to visible blue part of the spectrum. Fluorophores with longer

excitation and emission wavelength in the red and infrared part of the spectrum are frequently chosen as dyes in biological studies to reduce the background from autofluorescence. Thousands of different fluorophores are known, covering wide parts of the spectrum and providing variations in size, quantum yield, stokes shift and lifetime of the excited state. Exemplary, Cy5, a popular dye absorbing and emitting in the red part of the spectrum, is presented in Fig. 3. For the purpose of biosensing, the linking-chemistry to an assay, photo bleaching dose [1] and resistance to quenching effects are also important.

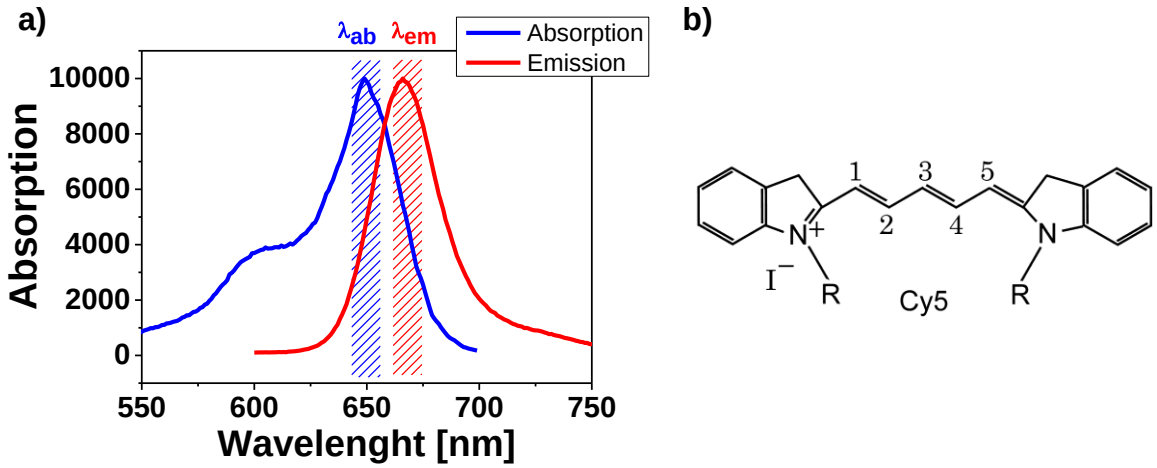

Fig. 3 Absorption and emission spectrum (a) of the Cy5 dye shown in (b)

Quenching

Phenomena competing with the radiative relaxation of an excited state, and therefore reducing the quantum yield of a fluorophore, are summarized under the term quenching.

The most important processes are internal conversion, collisions and Förster resonance energy transfer (FRET). FRET is a non-radiative energy transfer from an excited donor to an acceptor by dipole-dipole interaction. Characteristic is the conservation of the spin state in the transfer, which is mostly observed as singlet-singlet transition. While FRET has proven to be a valuable tool to measure intramolecular distances and molecular reactions with nanometer resolutions even in living cells [10], it imposes some limitation on fluorescence labeled assays. When the excited state of a fluorophore is transferred to an acceptor before fluorescence emission, the quantum efficiency is reduced. The FRET transfer rate

[1] By frequent excitation, fluorophores may be excited to a metastable state or rendered non-fluorescent. For ensembles of fluorophores, the dose at which the fluorescence intensity is halved is denoted photo bleaching dose.

follows coulomb characteristic

$$k_{FRET} = k_f \frac{R_{0,FRET}^6}{r^6}, \quad (2)$$

where k_f is the radiative decay rate of the donor and R_0 is the donor-acceptor distance at which 50% transfer efficiency is reached. For typical donor-acceptor pairs $R_{0,FRET}$ is in the order of 10 nm.

On metal surfaces an analog phenomenon is observed, called surface energy transfer (SET). The transfer rate follows a fourth power low

$$k_{SET} = k_f \frac{R_{0,SET}^4}{r^4}, \quad (3)$$

and shows larger interaction distances with typical $R_{0,SET}$ around 15nm, which is significantly larger compared to typical FRET distances [11]. These effects need to be considered in the design of fluorophore labeled assays on metallic surfaces or supported by metallic nanoparticles to avoid quenching of the fluorescence signal.

1.4. Plasmonic enhancement of fluorescence immunoassays

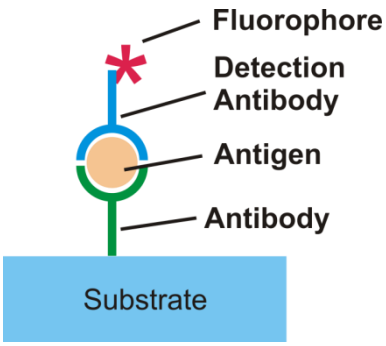

Fig. 4 Schematic of a sandwich immunoassay

Immunoassays are a large class of bioanalytical methods, where an analyte dissolved in a sample liquid is detected by a detection compound fixed to the sensor surface. Both, the antigen or the antibody can be used as recognition element to detect either antibodies or antigens in the liquid sample. To further enhance the signal, a secondary antibody labeled with a contrast enhancing dye may be attached on the captured analyte, forming a sandwich assay as shown in Fig. 4.

Plasmonic structures are an excellent tool to probe immunoassays due to the confinement and consequently strong enhancement of the plasmon field to a small volume covering the immunoassay, shown schematically in Fig. 5. With a typical size of antibodies of 10 nm plus an antigen, the fluorophore in a typical fluorescence labeled immunoassay is positioned 20 – 30 nm above the surface. This distance is a good compromise between the exponential decay of the

evanescent field of the surface plasmons, giving an enhancement of the fluorescence excitation rate $\frac{k_{ex}}{k_{ex,0}} = \left|\frac{E_{loc}}{E_0}\right|^2$, and the quenching by surface energy transfer to the metallic surface. Not only is the excitation rate enhanced but also the quantum yield of the dye, an effect that is stronger for lower quantum efficiency dyes. The effect is observed on continuous metal films layer with enhancement factors (EF) up to 30 [3]. Higher enhancement factors are reported for precisely

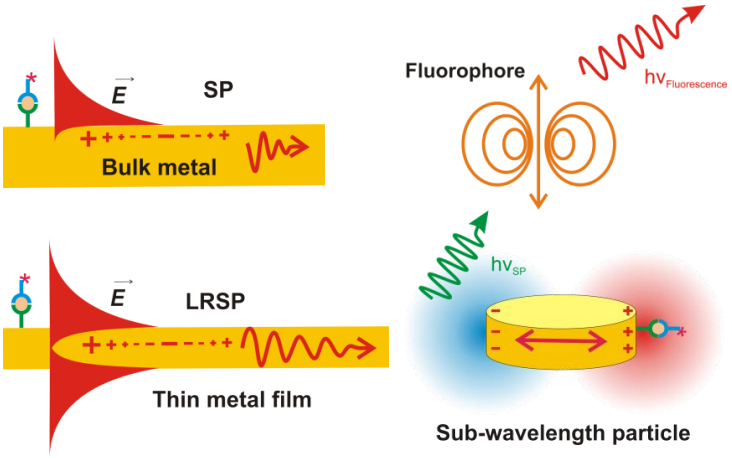

Fig. 5 Schematic representation of surface plasmon modes and the interaction with a fluorophore dipole moment

designed structures nanostructures, which exploit the enhancement of the electric field in gaps between metallic nanoparticles. In combination with surface plasmon coupled emission, enhancement factors in the order of 1000 have been reported [12].

2. Research goals

This thesis aims at the design, preparation and characterization of a new metallic nanostructure for surface plasmon-enhanced fluorescence biosensor application. The structure supports collective localized surface plasmons on diffractive arrays of metallic nanoparticles. These localized surface plasmons exhibit decreased radiative damping which is accompanied with stronger field enhancement than regular plasmonic nanostructures. Simulations will be pursued to identify geometries that provide distinct plasmonic resonances coinciding with absorption and emission wavelengths of red and near infrared fluorophore emitters. Based on this study, plasmonic nanostructures will be prepared and their morphological and optical properties investigated. In particular, the thesis focuses at following key aspects in surface plasmon-enhanced fluorescence spectroscopy:

- Identification of plasmonic structures which exhibit two surface plasmon modes at distinct wavelengths controlled by near field interaction between localized and propagating surface plasmons.
- Tuning the geometry in order to diffraction couple these plasmonic resonances to far field optical waves propagating normal to the surface for the future amplification of fluorescence signal in instruments with epi-fluorescence readout geometry.
- Identification of a plasmonic nanostructure geometry that can be prepared by mass production-compatible technology such as roll-to-roll with nanoimprint lithography (NIL).
- Preparation of the identified geometry and the morphological characterization in various preparation stages by atomic force microscopy (AFM) and scanning electron beam microscopy (SEM).
- Validation of the simulation approach by comparison of computed optical properties with experimental results and iterative optimization of the preparation procedure.

3. Theoretical background

3.1. Fundamental properties of light

The phenomena associated with light can be described by two fundamentally different physical models: As the propagation of electromagnetic waves or as uncharged, massless particles traveling at the speed of light *c*, the photons. The fundamentals of those two theories are linked by

$$\mathrm{E} = \mathrm{h}\,\nu, \tag{4}$$

$$\mathbf{p} = \hbar\,\mathbf{k}, \tag{5}$$

where h is the Planck's constant[2] and $\hbar = \frac{\mathrm{h}}{2\,\pi}$ the reduced Planck constant respectively, ν denotes the frequency of the electromagnetic wave and E refers to the kinetic energy of a photon. In the visible regime of about 400 to 700 nm the

[2] $\mathrm{h} = 6.62607004\ \mathrm{x}\ 10^{-34}\ \mathrm{m}^2\ \mathrm{kg}\ /\ \mathrm{s}$

energy E of a photon is in the range of about 1.7 to 3 eV[3]. The particle character of light is especially useful to describe the interaction of light with matter.

3.1.1. Maxwell equations

The interaction of the electromagnetic field with electrical charges and currents is described by four coupled partial differential equations, the Maxwell equations. Together with the equation for the Lorentz force and the principle of conservation of charge

$$\frac{\partial \rho}{\partial t} + \nabla \cdot \mathbf{J} = 0 \tag{6}$$

they form the foundation of classical electrodynamics and derived theories based on electrodynamics like optics and the theory of electrical circuits.

For the purpose of this thesis we will look at fields at sub-wavelength scales, but still much bigger than atomic lattice constants and will therefore use bulk parameters to describe material properties. While the microscopic Maxwell equations describe the interaction of the electromagnetic fields with all charges present, it is possible to split the charges and currents into external (an external driving force, for example an external field or current) and internal (the materials reaction) part [13]:

$$\rho_{tot} = \rho_{ext} + \rho \tag{7}$$

$$\mathbf{J}_{tot} = \mathbf{J}_{ext} + \mathbf{J} \tag{8}$$

where $\rho_{tot}, \boldsymbol{J}_{tot}$ refer to the overall charge and current in the calculation, ($\rho_{ext}, \boldsymbol{J}_{ext}$) are the external or source terms and ($\rho, \boldsymbol{J}$) denotes the internal charge and current as the systems response to the external stimuli.

Using this approach, the Maxwell equations result to:

$$\nabla \cdot \mathbf{D} = \rho_{ext} \tag{9}$$

$$\nabla \cdot \mathbf{B} = 0 \tag{10}$$

$$\nabla \times \mathbf{E} = -\frac{\partial \mathbf{B}}{\partial t} \tag{11}$$

[3] $1\ eV = 1.602176565(35) \times 10^{-19} J$

$$\nabla \times \mathbf{H} = \mathbf{J}_{\text{ext}} + \frac{\partial \mathbf{D}}{\partial \mathrm{t}} \tag{12}$$

In these equations the macroscopic fields of the dielectric displacement **D**, the electric field **E**, the magnetic field **H** and the magnetic flux density **B** are linked with the external charge and current density ($\rho_{\text{ext}}, \mathbf{J}_{\text{ext}}$).

The material response to applied fields can be described using the polarization **P** for electrical and the magnetization **M** for magnetic fields:

$$\nabla \times \mathbf{H} = \mathbf{J}_{\text{ext}} + \frac{\partial \mathbf{D}}{\partial \mathrm{t}}, \tag{13}$$

$$\mathbf{H} = \frac{1}{\mu_0}\mathbf{B} - \mathbf{M}, \tag{14}$$

with ε_0[4] and μ_0[5] being the electric permittivity and magnetic permeability of the vacuum respectively. The introduced polarization **P** is describes the density of internal electric dipole moments in the material and is linked to the internal charge density of the material by $\nabla \cdot \mathbf{P} = -\rho$ and to the internal current by $\mathbf{J} = \frac{\mathrm{d}}{\mathrm{dt}}\mathbf{P}$ as a consequence of the conservation of charge. It is well known, that the elementary electrical dipoles are randomly oriented in linear, isotropic materials in the absence of external electrical fields, resulting in an overall not polarized material. The presence of an external electrical field nevertheless, the elementary dipoles get aligned in the external field following a statistical distribution. In the approximation of weak fields, this process can be considered to be linear proportional to the applied field **E**, giving $\mathbf{P} = \varepsilon_0 \chi \mathbf{E}$ where χ denotes the electrical susceptibility, a dimensionless material constant. In the isotropic case χ can be considered to be scalar, but it is a tensor for anisotropic materials. Using the relative electric permittivity $\varepsilon = 1 + \chi$ the electric displacement can be rewritten as

$$\mathbf{D} = \varepsilon_0 \mathbf{E} + \mathbf{P} = \varepsilon_0 (1 + \chi)\mathbf{E} = \varepsilon_0 \varepsilon \mathbf{E}. \tag{15}$$

During this study, only nonmagnetic, isotropic materials will be considered, therefore the magnetization **M** will be neglected and the relative magnetic permeability will be considered to be unity μ=1.

As a physical process, the polarization of the material takes time, which results in

[4] $\varepsilon_0 \approx 8.854 \times 10^{-12}\ \frac{\mathrm{F}}{\mathrm{m}}$

[5] $\mu_0 \approx 1.257 \times 10^{-6}\ \frac{\mathrm{H}}{\mathrm{m}}$

the deviation from the ideal linear behavior which leads to the phenomenon of dispersion.

3.2. Surface plasmon resonance

The free electron gas density in a metal can be excited to collective oscillations versus the lattice atoms, called plasmons. On a metal-dielectric interface, surface modes exist, which exhibit exponential decay of the evanescent field into both materials, but oscillate in the interface plane. This class of modes, the surface plasmons also referred to as surface plasmon polaritons, tightly confines the field on the interface in the order of few hundred nanometers in the dielectric and tens of nanometers in the metal. The propagation length in the interface plane can reach in the order of 100 µm for excitation at optical frequencies. Particles of sub-wavelength dimensions in contrast are polarized in the external field, an effect known as localized surface plasmons *LSP*.

3.2.1. The wave equation

The derivation of the wave equation for surface plasmons on a metal – dielectric interface is presented in [13], which is taken as the guideline for the following section.

The curl equations 11 and 12 can be combined to

$$\nabla \times \nabla \times \mathbf{E} = -\mu_0 \frac{\partial^2 \mathbf{D}}{\partial^2 \mathrm{t}}. \tag{16}$$

This expression can be rewritten using the identities $\nabla \times \nabla \times \boldsymbol{E} = \nabla(\nabla \cdot \mathbf{E}) - \nabla^2 \boldsymbol{E}$ and

$\nabla \cdot (\varepsilon \mathbf{E}) = \mathbf{E} \cdot \nabla\varepsilon + \varepsilon \nabla \cdot \mathbf{E}$, with the assumption of negligible variations of the electric permittivity $\varepsilon(\mathbf{r})$ in the order of one wavelength, to the general form of a wave equation

$$\nabla^2 \mathbf{E} - \frac{\varepsilon}{\mathrm{c}^2} \frac{\partial^2 \mathbf{E}}{\partial \mathrm{t}^2} = 0. \tag{17}$$

With the assumption of a harmonic time dependence $\mathbf{E}(\mathrm{r}, \mathrm{t}) = \mathbf{E}_\mathrm{r}(\mathrm{r}) \mathrm{e}^{-\mathrm{i}\omega \mathrm{t}}$ and the introduction of the wave vector $\mathrm{k}_0 = \frac{\omega}{\mathrm{c}}$ of a propagating wave in vacuum, the equation simplifies to the *Helmholtz equation*

$$\Delta \mathbf{E} + \mathrm{k}_0^2 \varepsilon \mathbf{E} = 0\,. \tag{18}$$

For the next step, we consider the nature of the solution to this wave equation for surface plasmons: For simplicity reasons a plane electromagnetic wave on a surface in the x-y plane is propagating in the x direction is selected as starting point. Orthogonal to the propagation plane, the field distribution is not yet defined. Such a wave is can be described by $\mathbf{E}(\mathrm{x},\mathrm{z},\mathrm{t}) = \mathbf{E}(\mathrm{z})\, \mathrm{e}^{\mathrm{i}\,\beta\,\mathrm{x}}\mathrm{e}^{-\mathrm{i}\omega\mathrm{t}}$. Separation of the time component and insertion in 18 yields the wave equation

$$\frac{\partial^2 \mathbf{E}(\mathrm{z})}{\partial \mathrm{t}^2} + (\mathrm{k}_0^2\varepsilon - \beta^2)\mathbf{E} = 0. \tag{19}$$

The same result can be achieved for the **H**-field in an analog calculation. These two wave equations in combination with the curl equations (11,12) form a system of equations which supports two sets of self-consistent solutions, as shown in [13]. For the transverse magnetic (TM) solution only the field components E_x, E_z and H_y are nonzero while for the transverse electric (TE) solution only H_x, H_z and E_y differ from zero.

In the case of TM modes, the system of equations is reduced to

$$\mathrm{E}_\mathrm{x} = -\mathrm{i}\frac{1}{\omega\varepsilon_0\varepsilon}\frac{\partial \mathrm{H}_\mathrm{y}}{\partial \mathrm{z}}, \tag{20}$$

$$\mathrm{E}_\mathrm{z} = -\frac{\beta}{\omega\varepsilon_0\varepsilon}\mathrm{H}_\mathrm{y}, \tag{21}$$

with the wave equation

$$\frac{\partial^2 \mathrm{H}_\mathrm{y}}{\partial \mathrm{z}^2} + (\mathrm{k}_0^2\varepsilon - \beta^2)\mathrm{H}_\mathrm{y} = 0. \tag{22}$$

The analogue set of equations for TE modes is

$$\mathrm{H}_\mathrm{x} = \mathrm{i}\frac{1}{\omega\mu_0}\frac{\partial \mathrm{E}_\mathrm{y}}{\partial \mathrm{z}}, \tag{23}$$

$$\mathrm{H}_\mathrm{z} = \frac{\beta}{\omega\mu_0}\mathrm{E}_\mathrm{y}, \tag{24}$$

$$\frac{\partial^2 \mathrm{E}_\mathrm{y}}{\partial \mathrm{z}^2} + (\mathrm{k}_0^2\varepsilon - \beta^2)\mathrm{E}_\mathrm{y} = 0. \tag{25}$$

With these two sets of equations, solutions for the field components can now be determined, using the actual geometry of a problem.

3.2.2. Surface plasmons on a metal-dielectric interface

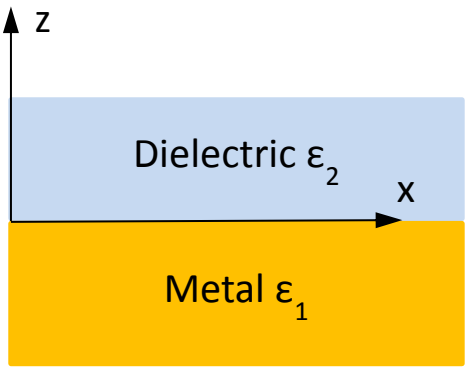

Fig. 6 Sketch of a metal-dielectric interface

The simplest geometry to support surface plasmon excitation is a two layer system of a weakly absorptive dielectric medium with dielectric constant $\varepsilon_2(\omega)$ where $\mathrm{Re}\{\varepsilon_2\} > 0$ and a conducive metal with dielectric constant $\varepsilon_1(\omega)$ with $\mathrm{Re}\{\varepsilon_1\} < 0$, which is implied by the metallic character (see Fig. 6). At first we will find a solution for the TM mode, using an ansatz for a propagating wave in x-direction and evanescent (= exponential decay) wave characteristics in the orthogonal z-direction. Solutions are formulated in each layer separately using constants, which are later determined by the boundary conditions on the interface. For the dielectric layer z > 0 the equations take the form of:

$$H_y(z) = A_2 e^{i\beta x} e^{-k_2 z}, \tag{26}$$

$$E_x(z) = iA_2 \frac{1}{\omega\varepsilon_0\varepsilon_2} k_2 e^{i\beta x} e^{-k_2 z}, \tag{27}$$

$$E_z(z) = -A_2 \frac{\beta}{\omega\varepsilon_0\varepsilon_2} e^{i\beta x} e^{-k_2 z} \tag{28}$$

and for the metallic layer z < 0:

$$H_y(z) = A_1 e^{i\beta x} e^{k_1 z}, \tag{29}$$

$$E_x(z) = -iA_1 \frac{1}{\omega\varepsilon_0\varepsilon_1} k_1 e^{i\beta x} e^{k_1 z}, \tag{30}$$

$$E_z(z) = -A_1 \frac{\beta}{\omega\varepsilon_0\varepsilon_1} e^{i\beta x} e^{k_1 z}, \tag{31}$$

where k_i is the wave vector component perpendicular to the interface. The penetration depth or evanescent decay length into the media is defined as $\hat{z} = \frac{1}{k_i}$ and describes the confinement of the wave to the interface.

Only in the case of $A_1 = A_2$ and

$$\frac{k_2}{k_1} = -\frac{\varepsilon_2}{\varepsilon_1} \tag{32}$$

the continuity of the tangential field components H_y and $\varepsilon_i E_z$ is fulfilled for nontrivial

solutions. It needs to be pointed out, that with the sign convention used in this calculation, the field is only confined to the surface if the condition $\mathrm{Re}(\varepsilon_1) < 0 \text{ if } \mathrm{Re}(\varepsilon_2) > 0$ or vice versa is fulfilled. This means, that surface plasmon modes only exist between interfaces with materials with opposite signs of the real part of the dielectric constant, i.e. a conductor and an insulator.

For the TM mode considered here, the magnetic field component $\mathrm{H_y}$ further has to fulfill the wave equation 22 which results in two equations, one for each half space:

$$\mathrm{k_1^2} = \beta^2 - \mathrm{k_0^2}\varepsilon_1, \tag{33}$$

$$\mathrm{k_2^2} = \beta^2 - \mathrm{k_0^2}\varepsilon_2. \tag{34}$$

These, in together with equation 32 can be combined to the dispersion relation for propagating surface plasmons at the interface between two half spaces

$$\beta = \mathrm{k_0}\sqrt{\frac{\varepsilon_1\varepsilon_2}{\varepsilon_1 + \varepsilon_2}}, \tag{35}$$

which is valid for both real and complex dielectric constants ε_1 which relates to ideal and conductive metals associated with dampening of the propagating plasmon.

The wave vector β is a complex value, where the real part $\mathrm{Re}\{\beta\}$ is associated with the wavelength of the surface plasmon and the imaginary part is related to the propagation length $\hat{\mathrm{L}} = \frac{1}{\mathrm{Im}\{\beta\}}$.

When a similar approach is used to solve the equations for transverse electric (TE) modes, the respective expressions for the field components are for z > 0:

$$\mathrm{E_y}(z) = \mathrm{A_2}\mathrm{e}^{\mathrm{i}\beta x}\mathrm{e}^{-\mathrm{k_2}z}, \tag{36}$$

$$\mathrm{H_x}(z) = -\mathrm{i}\mathrm{A_2}\frac{1}{\omega\mu_0}\mathrm{k_2}\mathrm{e}^{\mathrm{i}\beta x}\mathrm{e}^{-\mathrm{k_2}z}, \tag{37}$$

$$\mathrm{H_z}(z) = \mathrm{A_2}\frac{\beta}{\omega\mu_0}\mathrm{e}^{\mathrm{i}\beta x}\mathrm{e}^{-\mathrm{k_2}z} \tag{38}$$

and for z < 0:

$$\mathrm{E_y}(z) = \mathrm{A_1}\mathrm{e}^{\mathrm{i}\beta x}\mathrm{e}^{\mathrm{k_1}z}, \tag{39}$$

$$H_x(z) = iA_1 \frac{1}{\omega\mu_0} k_1 e^{i\beta x} e^{k_1 z}, \tag{40}$$

$$H_z(z) = A_1 \frac{\beta}{\omega\mu_0} e^{i\beta x} e^{k_1 z}. \tag{41}$$

Application of the boundary conditions, namely the continuity of E_y and H_x on the interface yield the condition

$$A_1(k_1 + k_2) = 0. \tag{42}$$

Since we are interested in surface plasmons, which are confined to the interface, the wave vectors in z direction k_z need to fulfill $\mathrm{Re}\{k_1\} > 0 \text{ and } \mathrm{Re}\{k_2\} > 0$, therefore equation 42 can only be fulfilled when $A_1 = 0$, which leads to $A_1 = A_2 = 0$ – the trivial solution. This means that *propagating surface plasmons only exist for TM polarization* [13]. The spatial electrical field distribution for a surface plasmon mode on a gold – water interface is shown in Fig. 7 for an excitation wavelength of 600 nm .

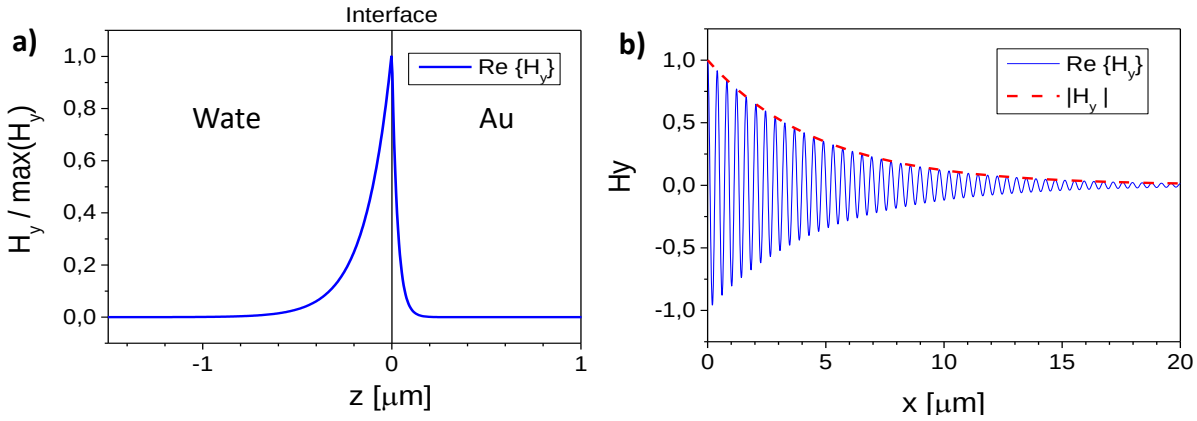

Fig. 7 Spatial field distribution for a surface plasmon mode on an Au - Water interface.

a) shows the evanescent field perpendicular to the propagation direction, **b)** shows the oscillating field and damping in propagation direction.

3.2.3. Localized surface plasmons

Localized surface plasmons are excitations observed on particles of subwavelength size, which do not support propagating plasmons but are rather polarized as a dipole in the external field. For a spherical particle with the dielectric constant ε_m embedded in a medium with dielectric constant ε, they can be described by Mie theory [13]. In this particular case and in the approximation of a particle diameter $a \ll \lambda$ Mie theory predicts the potential outside the particle to be

$$\Phi_{out} = -E_0 r \cos\theta + \frac{\mathbf{p} \cdot \mathbf{r}}{4\pi\varepsilon_0\varepsilon_m \mathbf{r}^3}. \quad (43)$$

With the polarization defined by $\mathbf{p} = \varepsilon_0\varepsilon_m\alpha\mathbf{E}_0$ the polarizability of the particle is found to be

$$\alpha = 4\pi\varepsilon_0\varepsilon_m a^3 \frac{\varepsilon - \varepsilon_m}{\varepsilon + 2\varepsilon_m}. \quad (44)$$

It is worth noting, that the polarizability is a complex value and proportional to the third power of the particle diameter *a* or its volume. From formula 44 it can be easily seen that for a minimum of $\varepsilon(\omega) + 2\varepsilon_m(\omega)$ the polarizability reaches a maximum. With the assumption of a slow varying absorption of the surrounding medium the *Fröhlich condition* for the dipole surface plasmon mode is derived

$$\mathrm{Re}\{\varepsilon(\omega)\} = -2\varepsilon_m. \quad (45)$$

When nanoparticles are arranged in a regular pattern, the localized surface plasmons can couple to form collective localized surface plasmons (cLSP).

3.2.4. Excitation of surface plasmons

The previous sections discussed the properties of surface plasmons as a polarization effect of the electron gas on a metal – dielectric interface. In order to resonantly excite surface plasmons in a metal, the incident light needs to match the surface plasmon in the oscillation frequency and the spatial wavelength. The connection between these is mathematically expressed in the dispersion relation. For light in a transparent dielectric, the dispersion relation is simply given by

$$\omega = c_m k \quad \text{or} \quad k = \frac{\omega}{c_m}, \quad (46)$$

where c_m refers to the speed of light in the medium $c_m = \frac{c_0}{n(\omega)}$. The dispersion relation for surface plasmons on a metal, dielectric interface was calculated in a previous section (equation 35) to be $\beta = k_0\sqrt{\frac{\varepsilon_d\varepsilon_m}{\varepsilon_d+\varepsilon_m}}$.

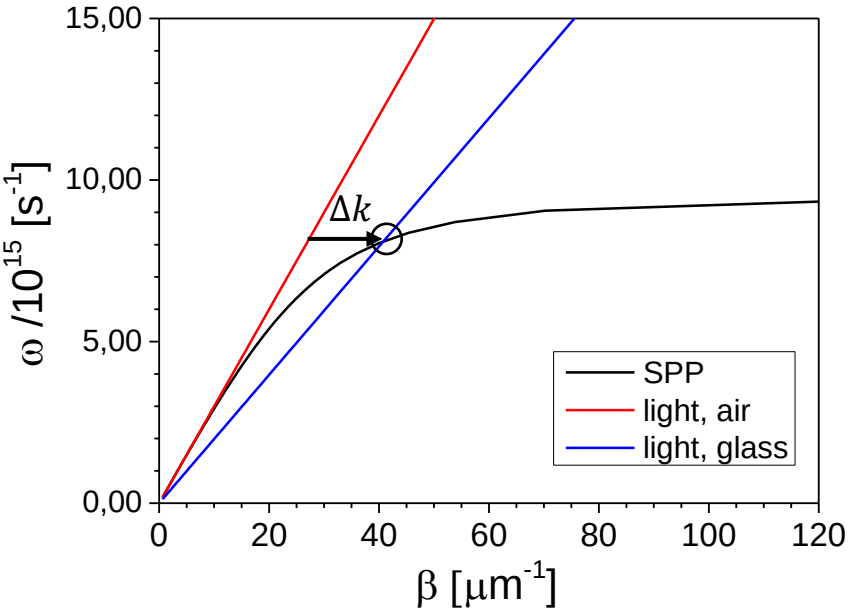

Fig. 8 Dispersion relations of a surface plasmon on a gold - glass (n=1.51) interface [black], light in air [red] and light in the glass blue]. The dielectric function of gold was modeled with the Drude model, with parameters taken from [22]

When looking at the dispersion relations Fig. 8 it is obvious, that the lines for the propagation of light in air and the surface plasmon never cross. This means that for no combination of k and ω resonant excitation of surface plasmons is possible. In a medium with refractive index n > 1, the wavelength of light at a given frequency ω is reduced compared to the vacuum conditions, which is visible in the graphic by the blue line, calculated for the propagation of light in a glass of refractive index n = 1.51. In this case, a resonant set of parameters exists – light can couple to surface plasmons.

The energy transfer to the surface plasmon and the subsequent absorption thereof in the metal layer is optically visible as a drop in the reflectivity of the otherwise reflective metal surface.

Practically, two methods of coupling are commonly used:

Prism coupling: In the Kretschmann configuration, the most widely used prism coupling setup shown in Fig. 9, the coherent incident light is made incident on a thin metal film through a prism. Surface plasmons are excited on both interfaces of the metal, allowing to probe the second interface through the metal film. The resonance of this coupled three layer system is very sensitive to each layers refractive index. Already subtle changes in the refractive index in immediate vicinity of the metal layer move the crossing point of the dispersion relations. In the Kretschmann configuration, phase matching between the incident light and the

surface plasmon is achieved by the variation of the angle of incidence or the excitation light's wavelength. Prism coupled systems exhibit surface plasmon resonances only at angles of incidence larger than the angle of total reflection.

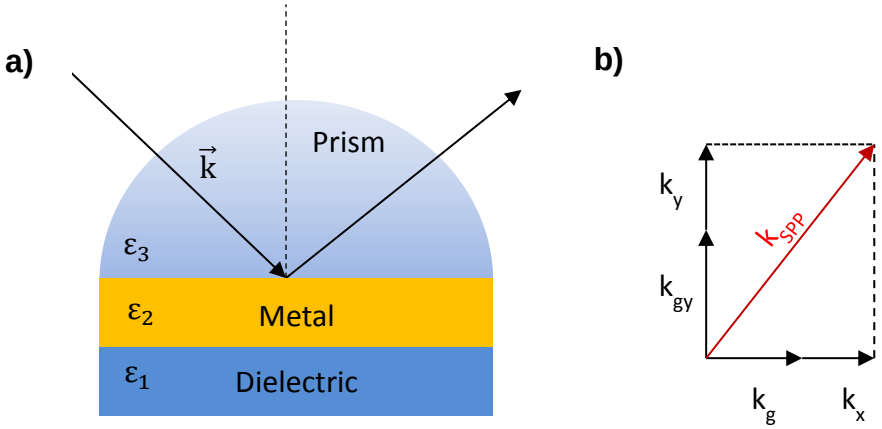

Fig. 9 a) SPR excitation using Kretschmann configuration, b) Wave vector addition for grating coupling

Grating coupling: Alternatively, a corrugated or regular patterned surface with period Λ may provide the missing momentum Δk by its grating vector $k_g = 2\pi/\Lambda$. Surface plasmon polaritons can be excited when the sum of the in-plane component of the incident light and the grating vector equals the surface plasmon momentum k_{SPP}.

To calculated the resonant grating period Λ, the grating vector components

$$k_{gx} = m\frac{2\pi}{\Lambda} \qquad \text{for} \quad m = 0, \pm 1, \pm 2, \ldots, \tag{47}$$

$$k_{gy} = n\frac{2\pi}{\Lambda} \qquad \text{for} \quad n = 0, \pm 1, \pm 2, \ldots \tag{48}$$

and the in plane components of the incident light

$$k_x = n_1 k_0 \sin\theta \cos\phi, \tag{49}$$

$$k_y = n_1 k_0 \sin\theta \sin\phi, \tag{50}$$

where n_1 is the refractive index of the material above the grating and θ is the angle of incidence, are inserted in the vector sum

$$k_{SPP}^2 = (k_x + k_{gx})^2 + (k_y + k_{gy})^2. \tag{51}$$

Inserting and solving the real part of the wave vector equation for the case of normal incident light ($\theta = 0, \phi = 0$) yields

$$\Lambda = \lambda_0 \frac{\sqrt{m^2 + n^2}}{\sqrt{\frac{\varepsilon_1 \varepsilon'_2}{\varepsilon_1 + \varepsilon'_2}}}. \tag{52}$$

4. Methods

4.1. Finite domain time difference simulations

Finite Domain Time Difference (FDTD) is a powerful numerical method to solve partial differential equations and is especially successful applied to study electrodynamic problems with complex geometries [14]. The key advantage of FDTD is an algorithm proposed by Yee [15] to solve the coupled curl equations of the Maxwell equations on two interlaced grids.

4.1.1. Theoretical background

The key idea of Yee's approach to the solution of the electromagnetic fields E and H is shown in Fig. 10. Each grid point of $\mathbf{E}_i$ is surrounded by four grid points of H_j necessary to calculate the curl equations in the form of

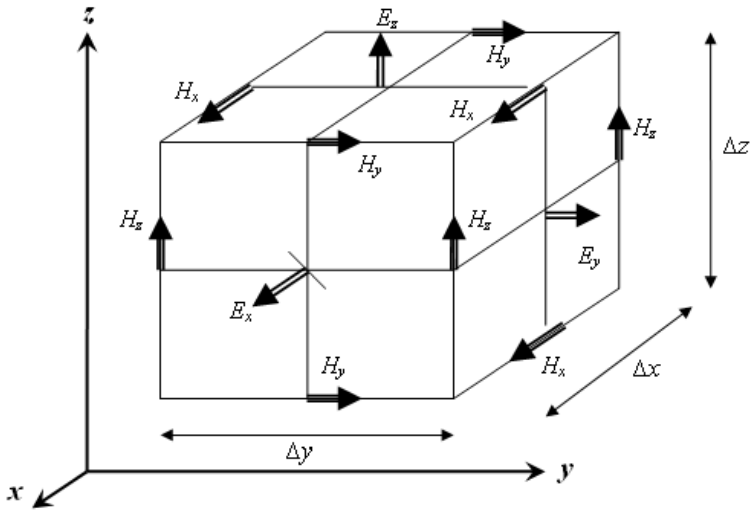

Fig. 10 Interlaced grids for E- and H-fields in the Yee algorithm [23]

Faraday's law

$$\frac{\partial \mathbf{B}}{\partial t} = -\frac{1}{\mu}\nabla \times \mathbf{E} - \frac{1}{\mu}(\mathbf{M} + \sigma^* \mathbf{H}) \tag{53}$$

and Ampere's law

$$\frac{\partial \mathbf{E}}{\partial t} = \frac{1}{\varepsilon} \nabla \times \mathbf{H} - \frac{1}{\varepsilon} (\mathbf{J} + \sigma \mathbf{E}), \tag{54}$$

where ε is the electrical permittivity, μ the magnetic permeability, $\mathbf{M}$ the magnetic current density, $\mathbf{J}$ the electrical current density, σ^* the magnetic loss and σ the electrical conductivity and vice versa. These two vector equations are a short notation for actually 6 equations for the field components. To solve this set of equations Yee's algorithm calculates the values of the H-field components at full time steps $t_n = n \cdot \Delta t$, while the components of the E-field are updated at time half steps $t_{(n+\frac{1}{2})} = (n + \frac{1}{2}) \cdot \Delta t$. To calculate, for example, the E_x field components at the location (i, j + 1/2, k + 1/2) at the time step $t = (n + \frac{1}{2}) \cdot \Delta t$, the H-field components are taken from the surrounding coordinates $H_y\left(i, j + \frac{1}{2}, k\right), H_y\left(i, j + \frac{1}{2}, k + 1\right), H_z\left(i, j, k + \frac{1}{2}\right), H_y(i, j + 1, k + \frac{1}{2})$ at the previous full time step $t = n \cdot \Delta t$. The H-field components at time step $t = (n + 1) \cdot \Delta t$ are subsequently calculated using the E-field components from $t = (n + \frac{1}{2}) \cdot \Delta t$. This spatial and temporal alternating method is a natural fit for the computation of solutions to the Maxwell equations. A detailed description of the formalism can be found in [14].

A significant advantage of FDTD compared to time independent methods like FEM is the capability to study large number of frequencies at once using a short excitation pulse, composed of a broad bandwidth of frequencies. After the solution of the equation in the time domain, the spectral behavior of the system is finally computed using Fourier transform.

The finite difference time domain method is implemented in a variety of software packages, most prominently MEEP [16], an open source package maintained by MIT and many more. For this work, the commercial software package fdtd-solutions from Lumerical was used, which provides a convenient graphical user interface and a selection of boundary conditions appropriate to study periodic plasmonic nanostructures.

4.1.2. Boundary conditions

In order to use the FDTD method to solve electrodynamic problems in a defined volume numerically, the area has to be filled with a computing grid. The number of

grid points is proportional to the volume and therefore scales with the third power of the spatial dimensions hence the computing volume has to be kept as small as possible, in order to save on computing time.

One of the most important problems in the definition of a simulation volume is the selection of boundary conditions on the simulation volume surface. Depending on the type of problem investigated, different behavior is needed and frequently even different conditions are chosen for different surfaces of the simulation volume.

Metallic

Metallic boundary conditions simulate a perfect conducting wall. Image charges will be simulated in the surface, which will exactly compensate the field. As a consequence, incoming electromagnetic waves are reflected on the surfaces with metallic boundary conditions.

Perfectly Matched Layer

To simulate open space conditions, a type of open boundary condition, that does not reflect or constrain electromagnetic waves in any way, is required. Several types of perfectly matched layer (PML) boundary conditions have been developed after the first version was introduced by Berenger in 1994 ranging from Berenger's initial split field approach over uniaxial PML to the more general stretched-coordinate PML. The key feature of PML boundary conditions is to not reflect waves on the non-PML to PML interface. This allows the PML volume to be strongly absorbing without consequences for the remaining computation volume. Due to the discretization of the wave, the PML conditions are not perfectly absorbing but slightly reflective. To reduce reflection in the computational volume, several layers of PML are stacked with increasing absorption coefficients.

Periodic

In many applications, the structures investigated are composed of a periodic repetition of unit cells. To reduce the computational effort it is highly advisable to exploit the periodicity of the structure by using periodic boundary conditions:

$$\mathrm{E}(\mathrm{x}+\Lambda)=\mathrm{E}(\mathrm{x}) \tag{55}$$

Periodic boundary conditions need to be applied in pairs on two opposing surfaces of the simulation volume and are limited to normal incident waves in optics simulations.

Bloch

Bloch boundary conditions are a generalization of periodic boundary conditions for incident waves at an angle θ_i . In this case, the boundary conditions are modified by a phase shift

$$\mathrm{E}(\mathrm{x}+\Lambda) = \mathrm{E}(\mathrm{x})\mathrm{e}^{-\mathrm{ik_x}\Lambda}, \tag{56}$$

where $\mathrm{k_x} = \mathrm{k_0}\sin\theta_\mathrm{i}$.

4.1.3. Simulation aims

The main strategies for improved performance in fluorescence assays are the increase of signal-to-noise (SNR) ratio of the fluorescent signal and a high collection efficiency for fluorescence photons. Bauch in his thesis [3] studies the parameters influencing the quantum efficiency, SNR ratio and directed emission of fluorescence light by nanoparticle arrays in detail. Here, a modified structure introducing an additional resonance due to manufacturing reasons is studied with respect of its viability for PEF.

The main sources of noise in a fluorescence signal are the detector dark count rate, residual fluorescence markers in the bulk water and auto-fluorescence of materials in the light path, limiting the SNR ratio. While the dark count rate is a camera property, which can be improved by cooling, the other factors need to be improved by experiment design.

The plasmonic confinement of the light to a small volume around metal interfaces and the associated increase in field intensity in combination with the functionalization of the metal interfaces with the fluorescent immunoassay has the potential to increase the fluorescence intensity of the sensor signal by orders of magnitude with respect to the not enhanced background light. This work focusses on the study of the plasmonic enhancement of the electric field intensity $|E|^2$ at 20nm above the metal particle surface, where the fluorophore of an immunoassay will be located in an optical near field study. The macroscopic parameter of surface reflectivity R will be calculated to provide a tool to evaluate produced nanostructures by optical measurements.

The resulting structure after the optimization process should fulfill following requirements:

- Plasmonic resonances at the absorption and emission wavelength of a fluorescent dye. The target dye for this study is Cyanin Cy5 dye with an emission wavelength of 666 nm and an excitation laser wavelength of 632 nm.
- Significant field enhancement at 20 nm above metal surface.
- Directed emission of fluorescence light.
- Simulation of far field reflectivity for experimental validation.

4.1.4. Investigated geometry

To economically optimize structures for plasmonic enhanced fluorescence, a simulation approach with subsequent experimental verification of the simulation results was chosen. In a previous work, Bauch [17] suggested an array of nanoparticles, excited to collective localized plasmon resonances (cLSP), as an efficient platform for plasmon enhanced fluorescence. A major shortcoming of the proposed structure is the incompatibility of the deposition of regular lattices of metal nanoparticle on flat surfaces with large scale mass production methods like roll-to-roll processes.

Here, a structure is proposed based on a regular pattern of polymer nanopillars with an evaporated layer of gold. By evaporation of a thin layer of metal on pillars, the metal accumulated on the pillar tops is separated from the continuous layer at

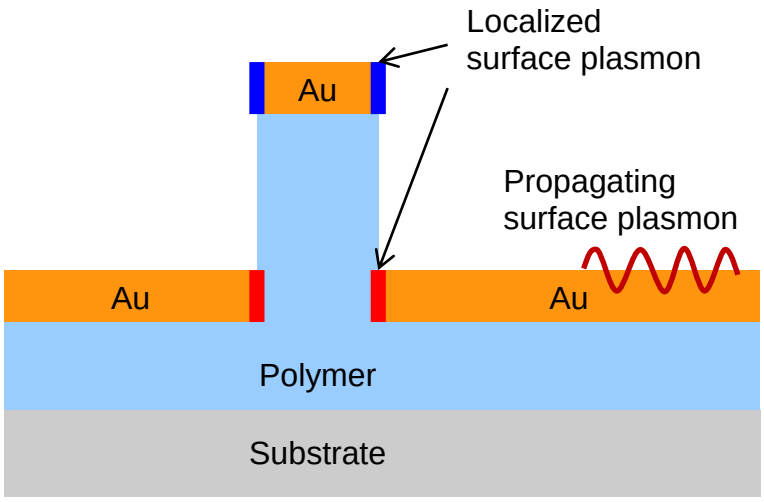

Fig. 11 Schematic cut through a nanopillar based plasmonic nanostructure.

the pillar base. The continuous metal layer is penetrated by the pillar base and forms an array of nanoholes.

Due to the close proximity to each other, the nanoparticle and nanohole resonances are expected to couple, with the coupling strength determined by the pillar height. The oscillations on single pillars are further coupled to each other by propagating surface plasmons, forming a complex optical system.

4.1.5. Simulation parameters

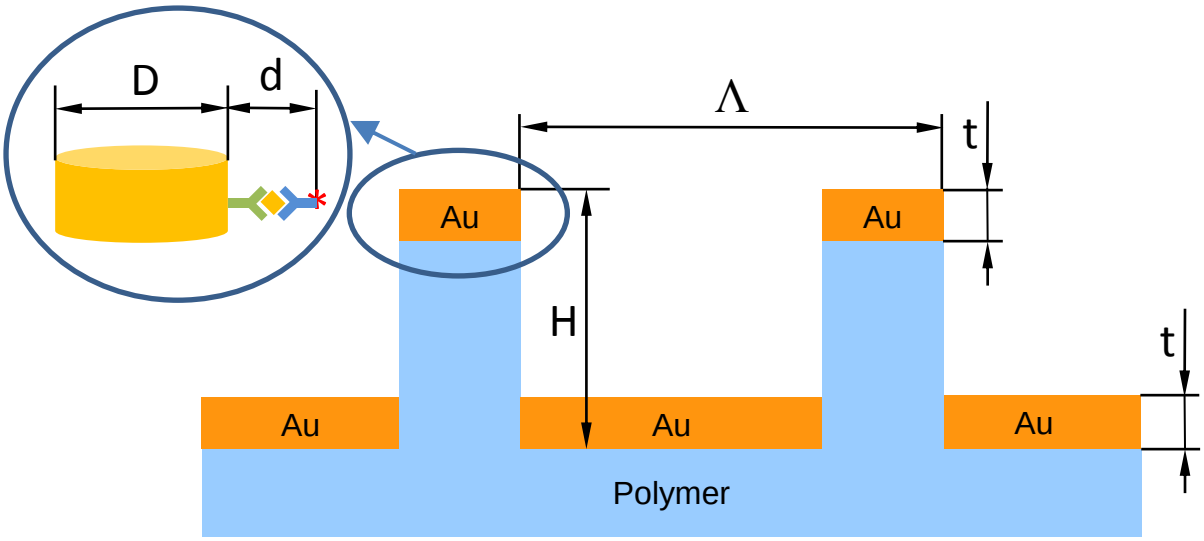

Fig. 12 Geometric parameter definitions

Geometry

Geometry parameters:

Symbol	Simulation parameter	Description
Λ	Simulation grid width	Grating period
D	d_particle, d_pillar	Particle and pillar diameter
t	h_particle	Metal layer thickness
H	h_pillar	Imprinted pillar height
d	x_probe	Fluorophore distance from metal surface

The periodicity of the pattern Λ in the simulation is defined by the unit cell dimensions in the pattern plane and the particle diameter is assumed to be equal to the supporting pillar diameter. For the simulation, the thickness of the residual

polymer layer was assumed to be larger than 300nm, which is significantly thicker than the penetration depth of the surface plasmons into the polymer. For this reason, the glass substrate shown in Fig. 11 was not considered in the simulation.

Materials

Gold: The fdtd-solutions integrated Gold (CRC)[6] model was used for the metal parts. It was fit in the $400\ \mathrm{nm} < \lambda < 1000\ \mathrm{nm}$ wavelength range using 6 coefficients.

Water: For the simulation of water, the integrated Water (Palik)[7] model based on the data of Palik.

Polymer: The supporting polymer was modeled by a non-dispersive, not absorbing dielectric with refractive index $\mathrm{n} = 1.51$.

Simulation setup

The simulations were performed on a regular rectangular grid with 2 nm grid resolution in all three dimensions. In the interface plane (x,y), the simulation volume was enclosed with Bloch boundary conditions with the dimensions $-\frac{\Lambda}{2} < \mathrm{x,y} < \frac{\Lambda}{2}$. Bloch boundary conditions are very similar to periodic boundary conditions but support plane wave sources with angle of incidence $\theta \neq 90°$. The z-dimension was chosen to be 1200nm, to provide sufficient spacing between the plane wave source and the structure to avoid direct interaction between the near field and the source as shown in Fig. 13. Perfectly matched layer boundary conditions were applied on the z axis, with 50 nm distance to the monitors in order to minimize artifacts from inevitable minimal reflections.

[6] CRC Handbook of Chemistry & Physics
[7] Handbook of Optical Constants of Solids I - III by E. Palik

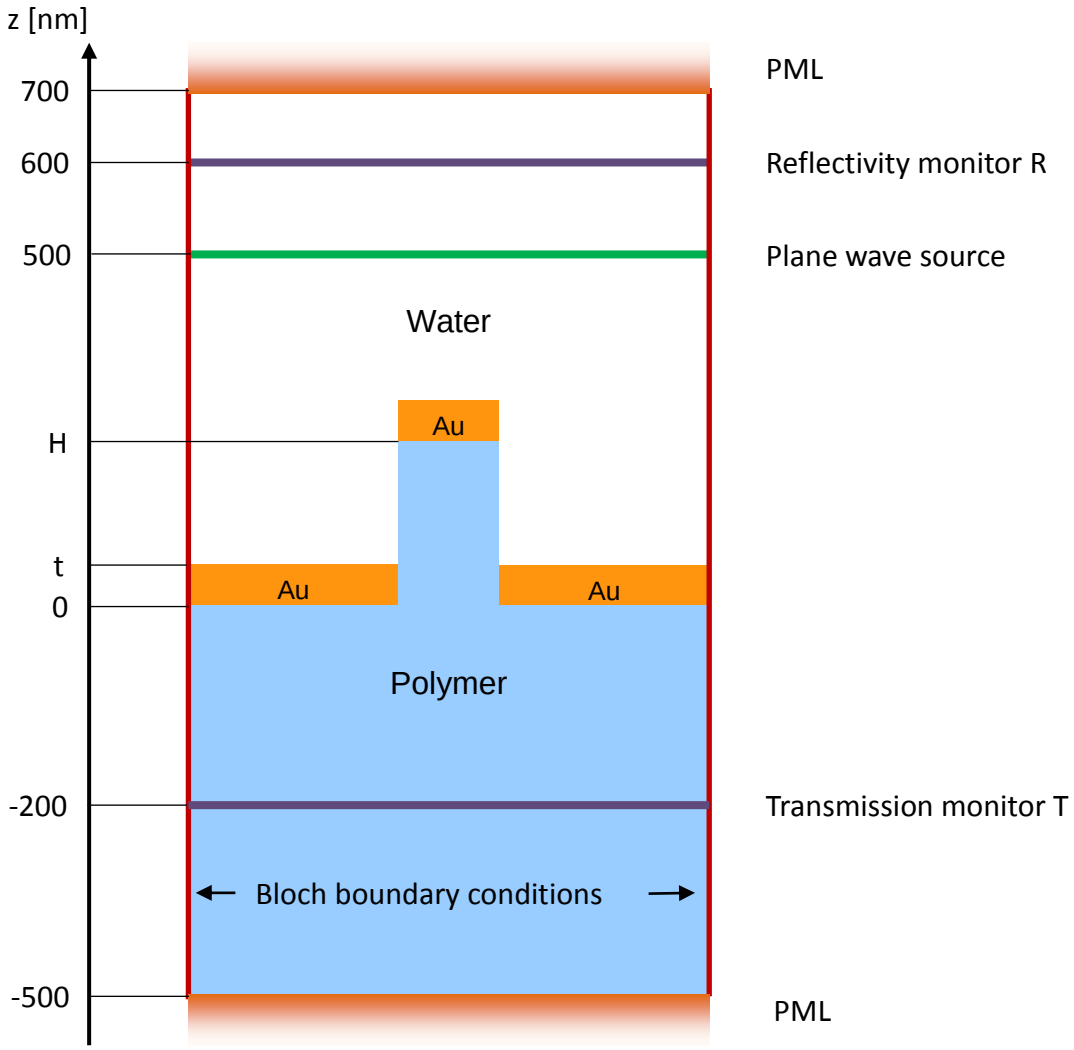

Fig. 13 Simulation boundaries and monitor locations

Symmetries

For normal incident light and periodic boundary conditions the simulation time is reduced by a large amount by the exploitation of symmetries. Typically, the computation time is reduced by a factor of 4-8. Special care has to be taken to select symmetries appropriate for the computational problem. The lattice geometry of the problem investigated in this study shows symmetry along two orthogonal axes, which for this consideration are assumed to be the x and y axes of the simulation volume, with the pillar structure placed in the center. By the illumination with polarized light, the symmetry of the problem is modified as shown in Fig. 14. A symmetric particle placed in the center (x=0, y=0), in an electric

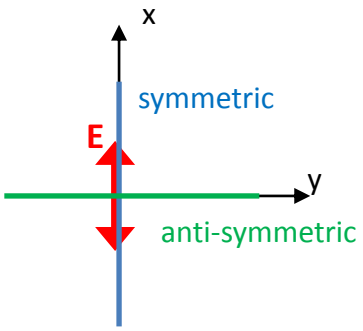

Fig. 14 Symmetry conditions with respect to the polarization of the normal incident light

field indicated by the red arrow, will be polarized and accumulates positive and negative charges on opposite sides of the y axes – the definition of anti-symmetry. This observation holds true for all electromagnetic fields in the volume, therefore the system excited with an E-field polarized in x direction exhibits symmetric behavior when mirrored on the x-axis and anti-symmetric behavior with respect to the y-axis.

Monitors

Due to the large size of the grid (at 2nm resolution in the order of $5 \cdot 10^6$ grid points) and the amount of data to store for each point (6 field components with min. 4 byte precision, resulting in a data volume of almost 100MB / time step for about 10.000 steps in one simulation) it is not possible to store the fields for the full volume during computation. Instead, only fields on 2D monitor planes are recorded for later evaluation. Fortunately, the nature of electrodynamic waves allows for near-to-far-field projections in homogenous, source free space, as explained in detail for numeric methods in [14]. Such a far field projection method is also implemented in the fdtd-solutions package.

To investigate the reflectivity R and transmission T, two 2D monitors parallel to the interface plane (x,y) were placed above and below the structure. The power transported through those surfaces, calculated in the form of the Pointing vector *S* is related to $\mathrm{R}(\omega) = \frac{\mathrm{S_R}(\omega)}{\mathrm{S_{source}}(\omega)}$ and $\mathrm{T}(\omega) = \frac{\mathrm{S_T}(\omega)}{\mathrm{S_{source}}(\omega)}$ respectively.

A third monitor was used in the light plane of incidence (x,z) recording the electrical field intensity at the symmetry axis y=0, which was used to study the field enhancement at the assumed fluorophore location.

Source parameters

A directional plane wave source aligned parallel to the metal-substrate interface with a wavelength range of $400\ \mathrm{nm} < \lambda < 1000\ \mathrm{nm}$ was placed 500nm above the interface to avoid direct interaction of the near field with the source. For comparison with angular resolved optical spectroscopy measurements, the source angle θ was varied but the source plane unchanged. In the case of tilted incident light, Bloch boundary conditions need to be used to account for the phase

difference on the boundaries.

4.2. Nanoimprint lithography

Nanoimprint lithography (NIL) refers to methods to structure surfaces by mechanical deformation of a soft or liquid layer on a substrate. The term was first coined by Prof. Stephen Chou et al. in a Science article in 1996 [18], demonstrating the production of 25nm structure size by a method later referred to as thermoplastic nanoimprint lithography. Many variations of the technique have been developed since, but all in common is the mechanical deformation of a soft substrate and subsequent curing. Popular variations include:

- Thermoplastic nanoimprint lithography (T-NIL): A thermoplastic substrate or a thermoplastic resist layer, spincoated on top the substrate, is heated to the materials glass transition temperature. When the temperature-resistant master is pressed into the thermoplastic layer, the imprint resist fills the molds surface structure with great precision. With the mold pressed on the surface, the assembly is cooled below the resists glass transition temperature and the stamp is removed, leaving a copy negative copy of the stamps pattern on the hardened surface. An inherent drawback of T-NIL is the potential distortion of the pattern by thermal expansion of stamp and resist layer.
- Photo nanoimprint lithography: In UV-cured photo nanoimprint lithography (UV-NIL), the usually transparent mold is pressed onto a low viscosity, photo curable, polymer which is spun on a substrate, with low pressure. With the stamp in place, the resist is cured by exposition to ultraviolet light. After curing, the mold is removed, leaving a negative pattern on the solid surface, as schematically shown in Fig. 15. The aspect ratios achievable in

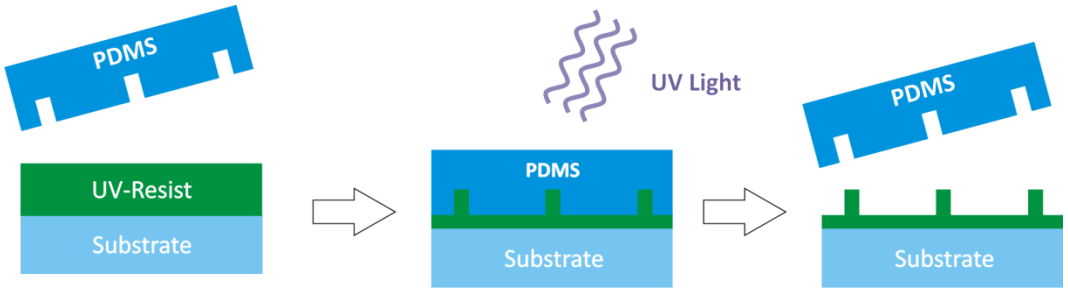

Fig. 15 Schematic of a UV-NIL process

this process depend on pressure, viscosity and surface energies of the stamp and the resist. A popular choice as mold material is poly(dimethylsiloxane) (PDMS) due to its excellent transparence in the UV.

Both presented versions of NIL processes may create a residual layer of resist, which covers the surface entirely but can be removed by etching processes or ion milling.

Nanoimprint lithography offers numerous advantages in microfabrication applications: Firstly, it is a cost effective method to create nanostructures on large surface areas. Large molds can be prepared using a step-and-repeat process to multiply a small, high resolution template, prepared by for example electron beam lithography, as demonstrated by Peroz et al. [19] for feature sizes down to 7nm. Further advantages are a good surface quality, especially low roughness, high fidelity and homogeneity, given constant pressure on the mold and compatibility with rigid and flexible substrates.

Industrial scale production

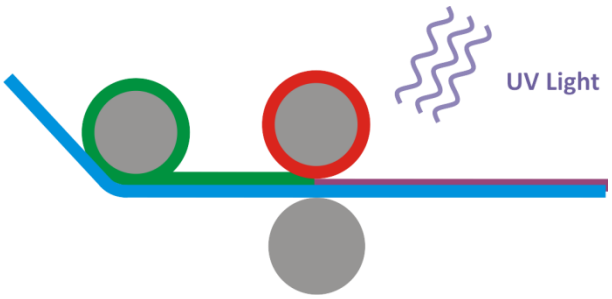

Fig. 16 Schematic of a roll-to-roll process for UV-NIL. A substrate polymer foil (blue) is coated with a thin layer of imprint resist (green), patterned by a nanostructured roll (red) and subsequently cured by UV light.

While on laboratory scale, patterns of up to few square centimeter can be transferred using PDMS molds, the process is also compatible with an industrial scale, continuous, roll-to-roll process. Roll-to-roll processes – as depicted schematically in Fig. 16 for UV-NIL – are capable of producing square meters of nanostructured areas within minutes. Most of the aforementioned advantages are valid for this approach but the aspect ratio of 3D structures is limited to about 1:1. Further processing steps, specifically coating and surface modification steps can be integrated in the process after structuring.

The structures investigated in this study were specifically designed for mass production, especially considering the requirements of roll-to-roll processes.

4.3. Metal layer deposition

For plasmonic surfaces the material quality is of high importance to avoid dampening, especially in highly resonant structures. For a metal layer, low surface roughness, high purity and large grain size are desirable to minimize losses [20]. In this study, gold (Au) was selected as thin film material for its good conductivity at optical frequencies and excellent chemical properties. The most important objective in the deposition phase was the preparation of Au nanoparticles on top of relatively low aspect ratio pillars, separated from a metal thin film at the pillar base. A thermal evaporator (Auto 306 TL400, HHV Ltd, UK) was used to deposit an adhesion layer of 2 nm Cr at deposition rates of 0.1 nm/s followed by the deposition of Au at rates of 0.1 nm/s in vacuum lower than 6 10^{-6} mbar. During deposition, the samples were mounted on a rotating holder at room temperature.

4.4. Atomic force microscopy

Since nanoimprint lithography is a method for topographic surface patterning, the results are characterized primarily using topographic tools. Atomic force microscopy (AFM) provides high special resolution on surfaces in all three dimensions on conducting and non-conducting surfaces and is therefore chosen as prime imaging method in this study. All measurements were acquired using a PicoScope scanning probe microscope (Molecular Imaging, Agilent (USA)), the AFM tips (PPP-NCHR from NANOSENSORS (CH) with force constant 42 N/m and resonance frequency around 300 kHz) used throughout this study are pyramidal shaped with a half cone angle of 10° and a minimum height of 10 µm.

Nevertheless there are some limitations associated with this method, which need to be considered for studies of the expected nanopillar patterns:

- AFM tips have a finite tip curvature of a few nanometers and are subject to wear, increasing the radius and therefore reducing the resolution during a measurement series. Any observed structure can be seen as a special convolution of the true surface pattern and the tip shape. This is not a

problem for low aspect ratio structures, where the surfaces angle, including the roughness, is lower than the half cone angle whereas for high aspect ratio structures like nanopillars, the observed edge steepness is limited as illustrated in Fig. 17.

- Another limiting factor to measure wall steepness with an AFM is the PID controller used to trace the surface. No PID controller is capable to follow an infinitely steep step on the input channel exactly. Instead, a characteristic step response function is observed, smearing out steep edges.
- Pillar height and top curvature are weakly affected by the effects discussed above but diameter measurements and wall shape estimation are.

Considering these arguments and the most important characteristics in regard of surfaces for plasmonic structures (pillar height, periodicity, surface roughness, pillar loss), AFM is chosen as the primary tool nanoimprint results investigation.

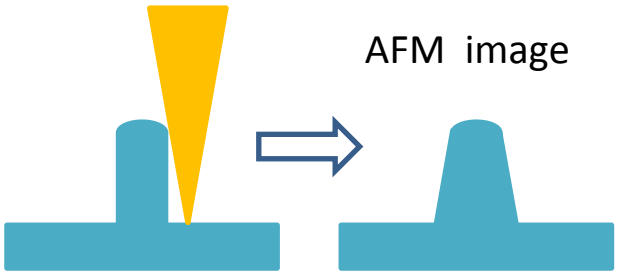

Fig. 17 Tip angle effect in AFM images

4.5. Angular resolved optical spectroscopy

The reflectivity of the plasmonic Au-nanostructures was investigated using a custom built angular spectroscopy setup (Fig. 18) assembled as follows: A white light source (halogen lamp LSH102 from LOT-Oriel) was connected to an optical fiber ML25L02 from Thorlabs (UK). An achromatic lens 14 KLA 001 CVI from Melles Griot (Germany) was used to collimate the light, which subsequently passed through a polarizer before it was directed towards the sample stage. The sample was mounted on a 2Θ rotation stage from Huber GmbH (Germany), contained in a flow cell which provided a window (SQ1, Hellma Optik (Germany)) for the incident and reflected beam. While one motor of the rotation stage was

used to control the angle of incidence *Θ* on the sample surface, the collection optics was positioned at a collection angle of *2Θ* by the second motor. A collimator (F810SMA-635 from Thorlabs (UK)) coupled the reflected beam into an optical fiber M26L02 from Thorlabs (UK) to direct the beam to a spectrometer HR4000 from Ocean Optics (USA). A software based on Labview (National Instruments (USA)) was used to control the data acquisition and control system. The typical measurement was recorded for angles *Θ* ranging from 1° to 12° with steps of 0.1°.

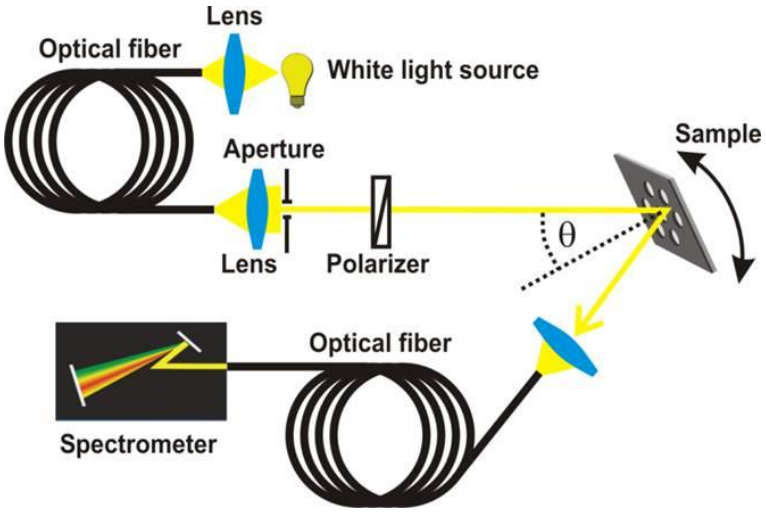

Fig. 18 Schematic drawing of the angular resolved spectroscopy setup

Due to the design of the reflectivity measurement setup, the starting angle was limited to 1°.

Measurement procedure:

1. Background measurement: With the incident light blocked before hitting the sample, a background reference spectrum $I_{BG}(\omega)$ was recorded to be subtracted from all following measurements. It accounts for any ambient light sources, leaked and scattered light from the system and the detector dark count. The background intensity was assumed to be independent of the angle.
2. Reference measurement $I_{ref}(\theta, \omega)$: In order to correct for the characteristic spectrum of the white light source, a measurement was taken on a reference spot on the sample. All samples were prepared in a way to provide an area of unstructured flat gold film as a reference spot.
3. Sample $I(\theta, \omega)$: Finally, the incident beam was moved to the nanostructured

area using an actuator stage and the spectra were recorded.

Following the acquisition, the reflectivity $R(\theta,\omega)$ was calculated from the three acquired spectra by:

$$R(\Theta,\omega) = \frac{I(\theta,\omega) - I_{BG}(\omega)}{I_{Ref}(\theta,\omega) - I_{BG}(\omega)}. \quad (57)$$

This normalization accounts not only for the white light source spectrum but also naturally removes the absorption associated with a thin film of gold from the resulting spectrum, leaving only the pattern effect. The same normalization has to be performed on simulated spectra in order to be directly comparable.

5. Materials

Ormostamp® imprint resist from Micro Resist Technology (Germany) was used for the production of working masters from the silicon waver negative. The Sylgard® 184 Silicone Elastomer Kit, Dow Corning (USA) was used to produce poly(dimethylsiloxan) stamps from the working masters. Nano imprint resists with high (Amonil© MMS1) and low (Amonil© MMS10) viscosity were purchased from Amo GmbH (Germany).

AFM images were recorded using a tapping mode Nanosensors PPP-NCHR tip with a tip radius < 10 nm and a half cone angle of 10°. The resonance frequency of this cantilevers is approximately 330 kHz with a spring constant k = 42 N/m.

6. Results

6.1. Simulation

6.1.1. Reflectivity dependence on the pattern periodicity

The structure was modeled as shown in Fig. 12 with dimensions selected according to Table 1, whereby the pattern period Λ was varied in the range from 400 to 500 nm in 5 nm steps, which are visible as a step structure in the results.

Table 1 Structure parameters for periodicity dependence study

Symbol	Value	Description
Λ	400 – 500 nm	Grating period
D	90 nm	Particle and pillar diameter
t	50 nm	Metal layer thickness
H	120 nm	Imprinted pillar height
d	20 nm	Fluorophore distance from metal surface

The resulting 20 spectra are shown in Fig. 19 summarized in one picture, with the reflectivity R as the color coded value. Each line in the figure corresponds to one spectrum R vs. λ.

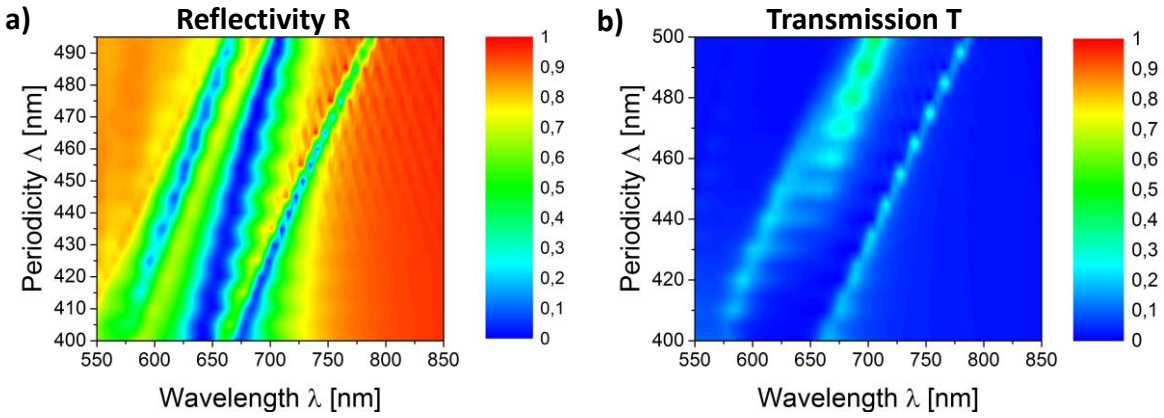

Fig. 19 Dependence of reflection (a) and transmission (b) spectra on the pattern period

Clearly, three minima of reflectivity are visible, all of which are shifted to longer wavelength with an increase of the structure period. As will be discussed below, the observed minima correspond to different resonant modes of the coupled oscillations. For two of the resonances also the intensity is dependent on the wavelength. At 460nm the two lowest wavelength resonances match with the absorption and emission wavelength of the Cy5 dye.

What is the reason for the minima in reflectivity? At those wavelengths, the excitation light efficiently couples to resonant surface plasmon modes of the structure. The electromagnetic field is confined at the metal surfaces where the energy is dissipated by the metal. As shown in Fig. 19 the transmission through the structure only accounts for 20% of the observed minima, peaking at around 40% for grating periods of 500nm. For the application in plasmon enhanced fluorescence transmission through the structure is undesirable, the electromagnetic energy should be either absorbed or reflected.

A cross-section through the near field at the symmetry plane (x,z) at y=0 (Fig. 20) for a structure with $\Lambda = 460\ nm$ provides the opportunity to study the optical near field.

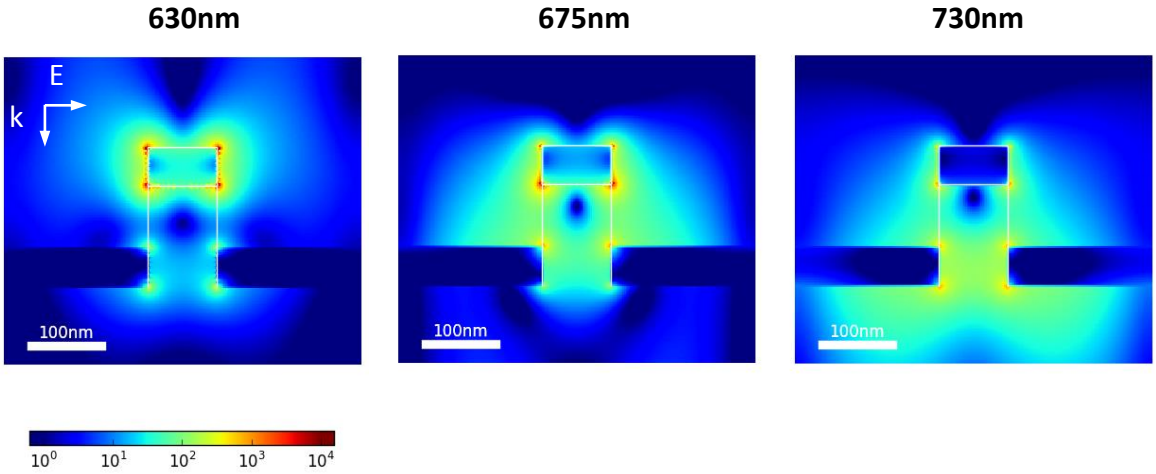

Fig. 20 Cross-section through the unit cell at y=0, showing the near field distribution of $|E/E_0|^2$ at three resonant wavelength of excitation light.

The three minima of R are clearly associated with resonant modes of the nanostructures. While the resonance at 630 nm is dominated by the particle polarization and the minimum at 730 nm is associated with the complimentary excitation of the nanohole, the absorption peak at 675 nm seems to be associated with a strongly coupled mode of particle and hole.

With respect to a sensing application, where the upper Au surfaces will be functionalized, the hole resonance is barely useful, since the field is confined within the supporting polymer. For the other two resonances, the intensity $\left|\frac{E}{E_0}\right|^2$ is increased by a factor of 20-150 at distances of 20 nm above the surface, which corresponds to the distance of a fluorophore form the surface in a fluorescent

immunoassay. Fig. 21 shows the close correlation between the microscopy parameter $\left|\frac{E}{E_0}\right|^2$ and the macroscopic parameter R. This relationship will be used to compare produced structures by optical measurements of R with the simulation predictions.

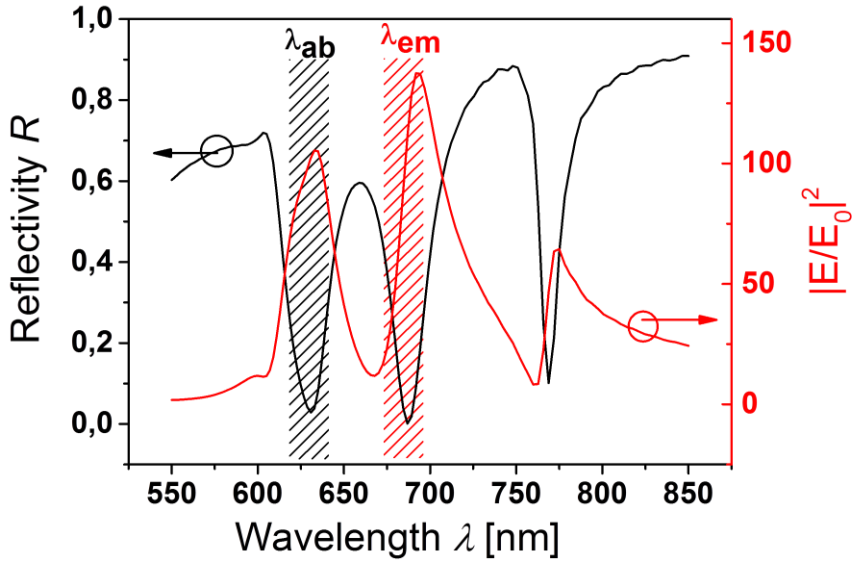

Fig. 21 Correlation between the near field property field intensity $\left|\frac{E}{E_0}\right|^2$ and the far field property reflectivity R

6.1.2. Pillar height study

A parameter which can be easily tuned experimentally is the pillar height or pattern depth of the imprinting process. The relation between pillar height and the resonant modes was studied in a system setup up with the parameters listed in Table 2, with a periodicity of 460 nm and a simulation resolution of 5 nm.

Table 2 Structure parameters for pillar height dependence study

Symbol	Value	Description
Λ	460 nm	Grating period
D	90 nm	Particle and pillar diameter
t	50 nm	Metal layer thickness
H	70 - 190 nm	Imprinted pillar height
d	20 nm	Fluorophore distance from metal surface

The resulting spectra are plotted in Fig. 22. Most notably, the position of the modes dominated by the localized surface plasmon resonances of the

nanoparticle (around 630 nm) and the nanoholes (around 740 nm) are weakly depending on the gap sizes h, except for small gaps of less than 40 nm. For the coupled mode in between, strong dependence on the gap height and subsequently the pillar height is observed.

This property provides means of tuning the structure to match the Stokes shift between absorption and emission wavelength for different dyes by tuning the pillar height.

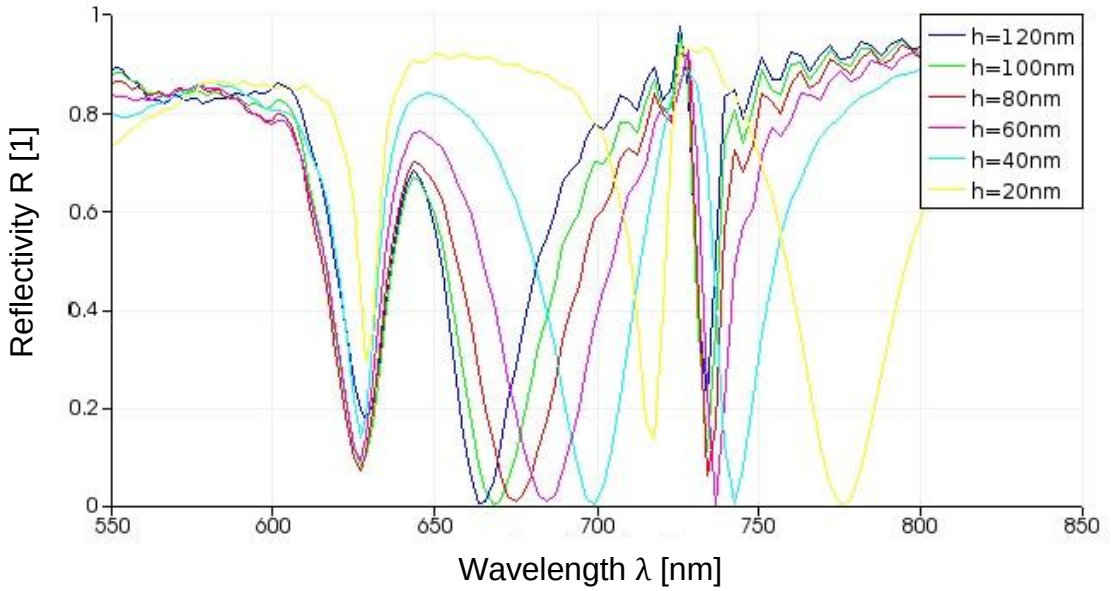

Fig. 22 Reflectivity spectral changes related to the pillar height. The height h noted in the graph is the gap height between the particle and the metal surface, $\mathbf{h = H - t}$.

6.1.3. Pillar diameter study

The pillar diameter is expected to be one of the most important parameters in the structure, since the localized plasmon resonances on particles and holes define the optical properties of the structure. To study the influence of the pillar diameters, a simulation was set up using the parameters given in Table 3 to investigate pillars and the associated holes with diameters from 60 – 150 nm. For the computation the particle and hole diameters were assumed to be equal. Further the gold layer thickness was assumed to be constant on top of the flat pillar top and on the base gold layer to the pillar circumference.

Table 3 Structure parameters for pillar diameter dependence study

Symbol	Value	Description
Λ	460 nm	Grating period
D	60 - 150 nm	Particle and pillar diameter
t	50 nm	Metal layer thickness
H	160 nm	Imprinted pillar height
d	20 nm	Fluorophore distance from metal surface

The results of the pillar diameter study are summarized in Fig. 23. For diameters of 90 nm the three resonances for the two localized and the strongly coupled mode are clearly visible. Towards smaller particle size, the absorption of the structure at all resonance frequencies is reduced. The LSP mode with the shortest wavelength, associated with the nanoparticle, shows a linear dependence on the particle diameter. The other two modes show a significantly stronger dependence on the particle size, where the mode with the longest wavelength, associated with the LSP of the nanoholes, is especially narrow.

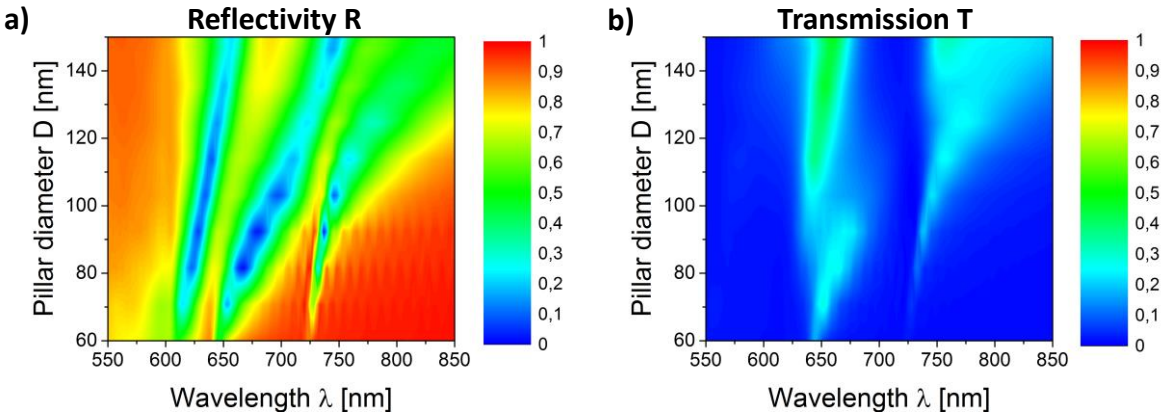

Fig. 23 Dependence of reflection (a) and transmission (a) spectra on the pillar diameter

6.2. Experimental

6.2.1. Preparation of polymer nanopillars

As master for the experimental structure production, a monocrystalline silicon wafer was prepared by electron beam lithography (EBL) with a regular array of holes with 90 nm diameter, 260nm depth and a periodicity of 460 nm in both directions and coated with an anti-adhesion layer of perflurosilane by Temicon

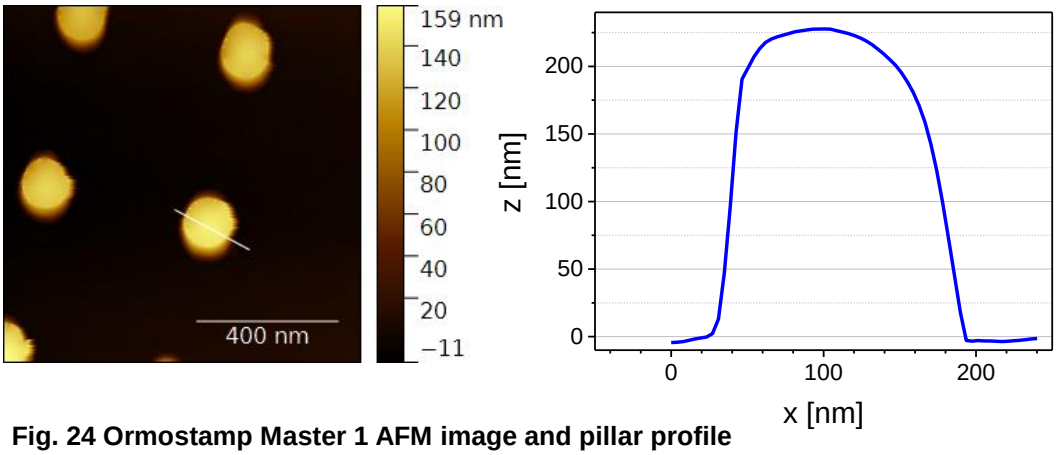

Fig. 24 Ormostamp Master 1 AFM image and pillar profile

GmbH (DE). In order to limit the risk to the silicon master carrying the negative pattern, positive working copies were created by Federica Pirani using OrmoStamp UV curable imprint resist. Four of those positive patterned stamps were used throughout further studies as masters for the PDMS working stamp production. A profile depth (pillar height) of more than 200nm was verified by AFM measurements with a typical pillar profile shown in Fig. 24.

In the next step, a PDMS stamp was prepared from Sylgard 184 from Dow Corning (USA) using a mixing ratio of 1:10 with its curing agent. It was poured over the patterned Ormostamp and cured without evacuation for 48h at 25°.

Next, a low viscosity nanoimprint resist (Amonil© MMS10, Amo (Germany)) was spun on a BK7 glass slide at 2000 RPM for 60 sec with 4 sec ramp time for an expected layer thickness of 180nm. The pattern was imprinted using the PDMS stamp and cured in an UV-crosslinker (Vilber Lourmat, DE) at 10 J/cm².

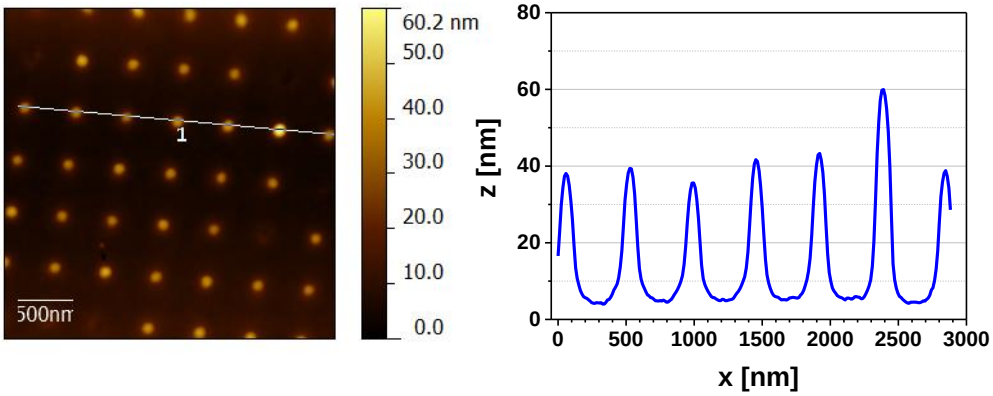

Fig. 25 AFM image and pillar profile along the indicated line of an imprinting sample prepared with a low viscosity imprint resist MMS10

Table 4 Low viscosity imprint resist (MMS10) pillar statistics

Parameter	Value
Average pillar height	31.2 +/- 5 nm
Pillar loss ratio	0.125

As shown in Fig. 25, the nanoimprint resist did not fill the pattern in the PDMS stamp efficiently, resulting in a profile depth of only 31 nm with high variation and 12.5% loss rate of pillars.

To increase the amount of material available to form the pattern, the higher viscosity imprint resist Amonil© MMS1 was chosen for the next production batch. 200ul of MMS1 resist were spun on a 20 x 20 mm glass substrate at 4000 RPM for

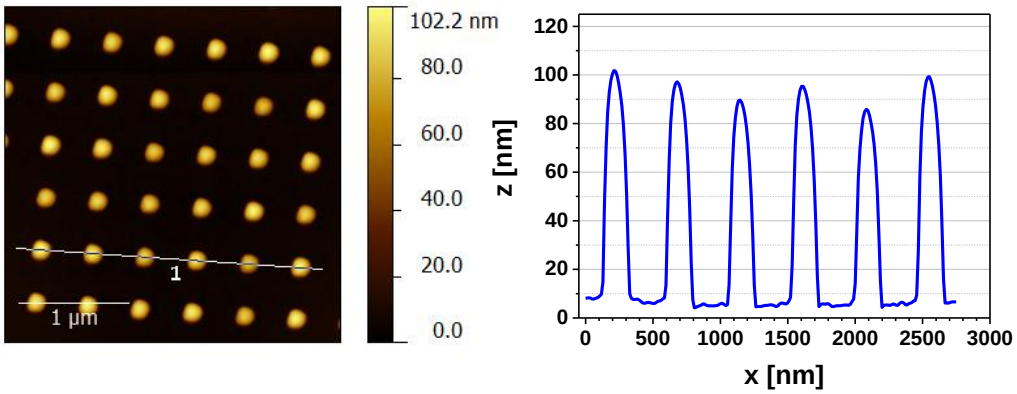

Fig. 26 AFM image and pillar profile along the indicated line of an imprinting sample prepared with a high viscosity imprint resist MMS1

60 sec with 4 sec ramp time for an expected layer thickness of 830 nm, which is significantly higher than the design pattern and is intended to provide sufficient excess material to slowly fill the patterned pores in the PDMS stamp. Immediately after imprinting, the resist was cured in a UV-crosslinker, using a dose of 10 J/cm².

Table 5 Pillar height statistics of samples imprinted in MMS1, cured immediately after imprinting.

Sample	Pillar height
A1.2.1	109.7 +/- 8.64 nm
A1.2.2	81.62 +/- 14.25 nm
A2.2.1	83.68 +/- 9.42 nm
A3.2.1	90.22 +/- 4.74 nm

The use of higher viscosity imprint resist with its resulting increased layer thickness of liquid resist for imprinting lead to a significant increase of the average pillar height. As shown exemplary in Fig. 26 the homogeneity of the imprinted pattern increased as well. Nevertheless the observed pillar height was found to be insufficient meet the design requirements. Considering the geometry of the stamp, a PDMS block with nanoholes of 90 nm diameter and 220 nm depth, trapped air in the far end of the hole is suspected to prevent the imprint resist to fill the holes. Therefore, to further improve the imprinting process, a degassing step was added to the protocol:

After the careful imprinting of the PDMS stamp into the liquid resist layer, the sample with stamp was moved into a vacuum chamber to degas with slowly decreasing pressure for more than one hour at a final pressure of less than 100 mbar.

As shown in Table 6 Extended degassing results, the improved degassing process increased the average pillar height not significantly and, as shown in the direct comparison on sample A3.2.3, the tip condition has negligible influence on the observed pillar height.

Table 6 Extended degassing results

Sample	Pillar height
A2.2.3 old AFM tip	93.48 +/- 10.73 nm
A3.2.3 old AFM tip	98.41 +/- 9.28 nm
A3.2.3 new AFM tip	100.77 +/- 9.43 nm

Investigation of the pillar diameters shows that the biggest impact on observed pillar diameters can be contributed to the wear of the AFM tips during the imaging process, as shown in the direct comparison between images of the sample A3.2.3.

In addition to the known tip angle, and therefore known broadening of the pillars, adhesion of material during the imaging process as well as breaking of the tip can increase the observed diameters. For these reasons, pillar diameters acquired by AFM imaging have to be interpreted as an upper boundary limit of the true pillar diameter.

6.2.2. Metal layer deposition

The target design requires the evaporation of 50 nm of Au on imprinted nanopillars of 160nm height in order to create 50 nm nanoparticles coupled to a 50 nm Au layer, with nanoholes enclosing the pillars, to couple the particles localized plasmon excitations by propagating surface plasmons. Due to the small pillar height of 80 - 100 nm, achieved in the imprinting process, the amount of deposited gold was reduced to 30 nm in order to proof that the production of nanoparticles separated from the continuous layer is feasible with this production method. As a consequence, the optical properties are significantly different from the designed structure.

Following a 2 nm Cr adhesion promoting layer, 30 nm of Au were deposited on the structure using a thermal evaporation system (HHV FL400) at a deposition rate of 0.1 nm/s. The low deposition rate was selected to ensure low surface roughness on the continuous metal layer and to avoid the formation of metal islands. The surface roughness of the gold layer between the pillars was measured with the AFM and found to be smaller than 2.1 nm RMS.

To estimate the nanoparticle height, the pillar height was measured before and after deposition. Different layer heights on the top of the pillars and the bottom continuous layer would result in a change in the average pillar height. As shown in Fig. 27, the mean pillar height changed by 8 nm in the sample A2.2.1, which is within the margin of error of the measurements. No change was observed in sample A3.2.1 indicating a homogenous deposition of Au on and around the pillars.

To prove the separation of the nanoparticles on top and the continuous layer on the bottom, the samples were subsequently investigated using a Scanning Electron Microscope (SEM) (Zeiss Supra 40 VP). Firstly, the pillar loss rate in the imprinting process was estimated by the imaging of a random area as shown in Fig. 28 (b) and comparing the number of pattern defects in relation to the total

number of pillars on the image. According to this procedure, the pillar loss ratio in the imprinting process was 6.1%.

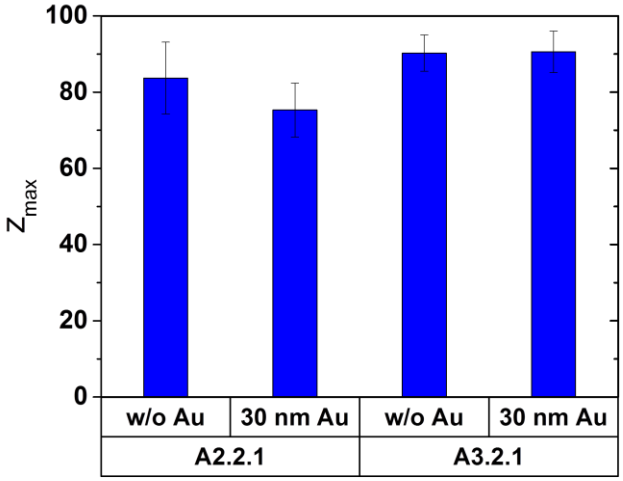

Fig. 27 Pattern height before and after Au deposition. No significant change in the average pillar height is observed, suggesting homogenous Au layer thickness on the pillar caps as in the surrounding area.

Secondly, the electrical insulation of the particles was investigated. Fig. 28 (a) shows an orthogonal image of the nanoparticles on sample A3.2.1. The bright color of the particles in the InLense detector image indicates charging of the nanoparticles, which suggests the electrical insulation of the particles from the continuous conductive layer.

This high contrast mode was used to measure the average pillar diameter using the software ImageJ. After application of a threshold function the particles were

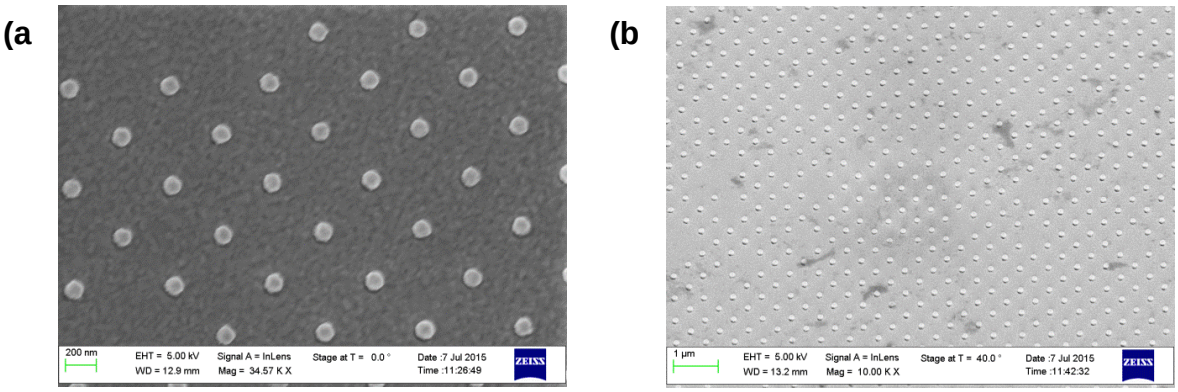

Fig. 28 SEM images of Au coated nanopillars.(a) InLense detector indicates charging of the nanoparticles, while the observed loss rate of pillars is 6.1% in (b).

detected using a clustering algorithm with a lower limit of particle size of 200 nm²

while ignoring all particles touching the image edges. Subsequently, the boundaries of the detected particles were fit with an ellipse, taking the major axis length as the particle size. Using this procedure the average particle diameter was estimated to be 124.4 +/- 3.1 nm.

The separation of the particles formed by the deposited gold on top of the pillars and the layer surrounding the pillars is confirmed visually using SEM images with the sample tilted 40° from the horizontal plane, as shown exemplary in Fig. 29. Most importantly, a dark gap, the polymer pillar, separates the bright metal areas. The random formation of nanoparticles of diameters around 10 nm is observed consistently on the sidewalls of all pillars investigated. Further studies will be required to investigate the effect of these particles on the sensing performance. Furthermore an umbrella effect of the gold cap is observed on the underlying nanoholes, leading to a reduced gold layer thickness in the nanopillar vicinity and an increased nanohole diameter. The increase deposition of metal to the pillar caps and associated increased nanohole diameter may cause a shift of the associated resonances towards longer wavelengths and need to be considered in future designs.

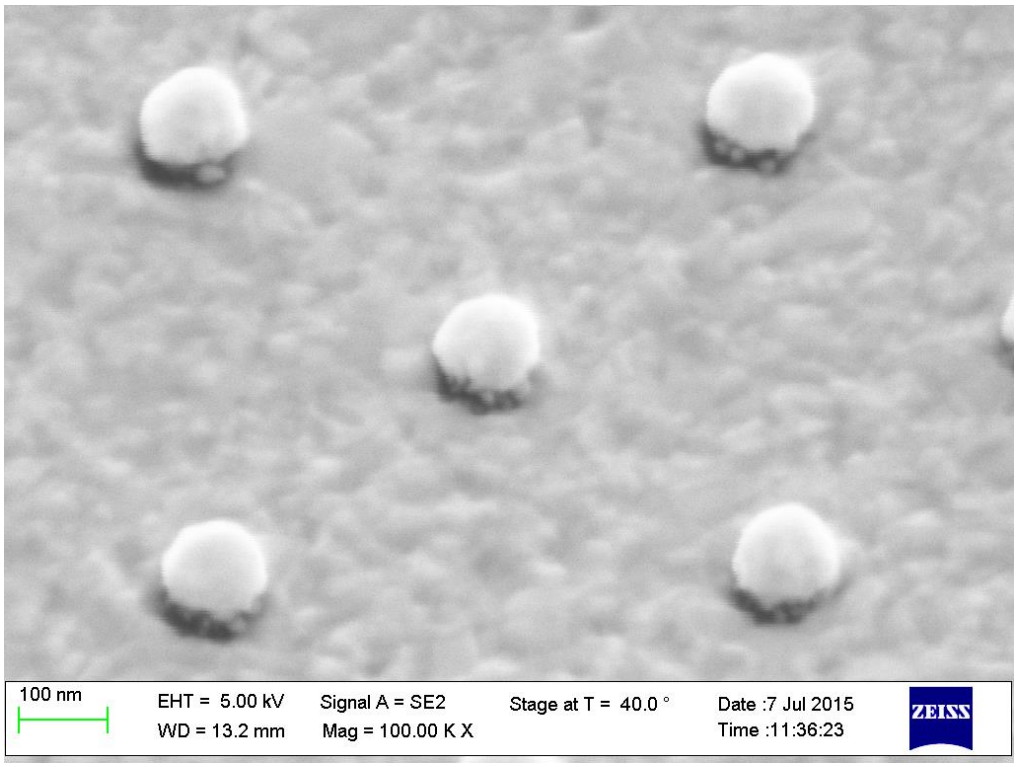

Fig. 29 Nanoparticles on top of MMS-1 pillars, separated from the continuous conductive layer imaged at an angle of 40°. The average gap distance is estimated to be 31.4 +/- 4.3 nm. Small nanoparticles of diameters around 10 nm are visible on the pillar walls.

6.2.3. Optical characterization

In order to evaluate the produced structure respect to its application, reflectivity was chosen as optical parameter to compare the structure with the simulation results. For the reflectivity measurement, performed on a setup described in the methods part in section 0, the sample was placed in a flow cell and aqueous environment. The reference measurement was performed on an unstructured area on the same sample. Following the reference measurement, the beam was moved on the structured area using an actuator stage and the measurement sequence was repeated. Subsequently, the angular resolved spectra from the sample area were divided by the spectra acquired on the reference area to isolate the pattern effect. The acquired TE spectrum is shown in Fig. 30a in direct comparison with the initial design goal. Clearly, three characteristic resonances are visible in the experimental spectrum as well as in the design spectrum. Due to the deviations from the design goal in the production process, namely the reduced pillar height and therefor increased coupling between the cLSP and the PSP and the increased particle size, the positions of the resonances are shifted towards the infrared. In order to validate the simulation approach, an approximation of the prepared structure was simulated to compare with the results from the optical measurement. The results are plotted in direct comparison with the experimental spectrum in Fig. 30b. To produce this simulation the pillar height was chosen to be 90 nm with a pillar top radius of 50 nm. The gold nanoparticle on top of the pillar was approximated by an oblate spheroid with 120 nm diameter in the horizontal plane and 100nm in the vertical direction as depicted in Fig. 32.

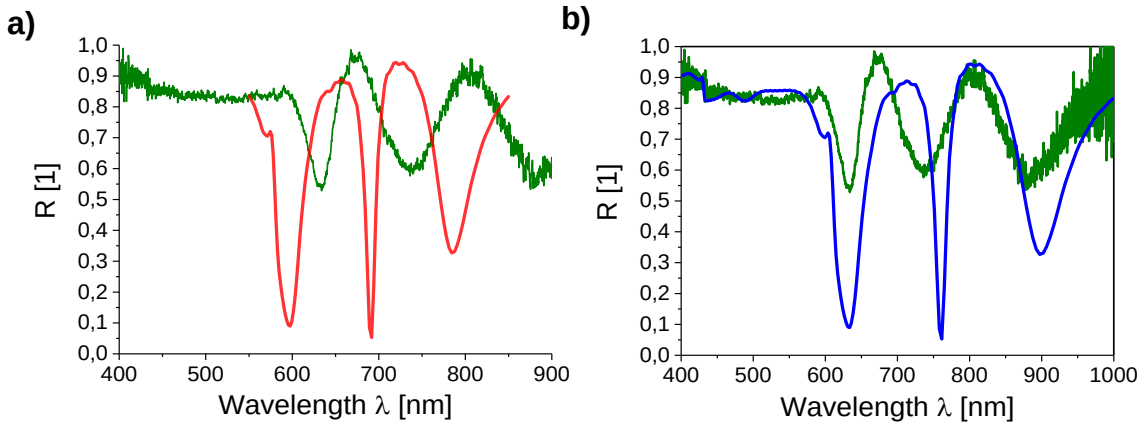

Fig. 30 Comparison of a) measured TM reflectivity spectra at 1° angle of incidence and computed spectra for the target structure (red) and b) a simulation using the structure parameters experimentally determined by AFM and SEM.

In the angular spectroscopy measurement, spectra are recorded for varying angle of incidence. Since propagating surface plasmons are can't be excited by TE polarized light, absorption peaks are related to localized surface plasmons only and are not depending on the angle of incidence, as observed in Fig. 31a,b. The three resonances are visible and show no shift over the angle of incidence.

For TM modes, shown in Fig. 31c,d the resonances are less pronounced, especially the nanohole associated mode is observed to be weak. The nanoparticle mode shows a linear relationship to the angle of incidence, which expected for a grating coupled mode.

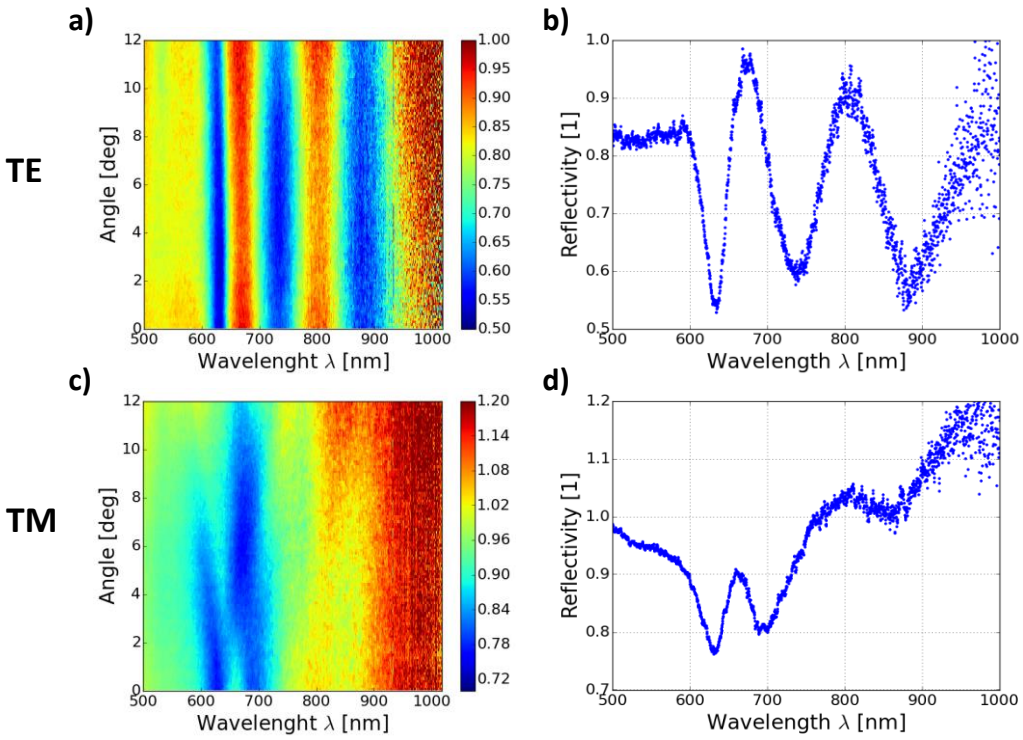

Fig. 31 Angular resolved spectra for TE (a,b) and TM (c,d) modes

The spectra b, d were taken from 1° angle of incidence measurement.

6.3. Summary

Simulations show, that a structure composed of an array of metallic nanoparticles and a mirror plane exhibit three surface plasmon resonance modes. These modes are tunable by geometric parameters, namely the particle diameter, the pillar height, pattern periodicity and metal layer thickness. While diameter and periodicity affect all three modes in a similar manner, the pillar height affects the coupled mode stronger than the others, allowing the tuning of resonances spectral distance.

It was proven, that by the method of nanoimprinting with subsequent deposition of a metal layer, nanoparticles separated from a nanohole array can be produced. The results of the investigation of the structure are summarized in Fig. 32. Firstly, the desired pillar height of 160 nm was not achieved in the NIL process and therefore a thinner layer of 30 nm gold was deposited. Further, the pillar tops are not flat as assumed in the initial simulations, but show significant curvature in the AFM images. SEM images also show a diameter of 120 nm of the gold nanoparticle with curved top, which corresponds to a mushroom like structure, as visualized in the figure. Further, smaller nanoparticles of diameters in the order of 10 nm and below were observed on the polymer pillar walls.

Due to these deviations from the target structure, the optical characteristics of the structure differ from the target design.

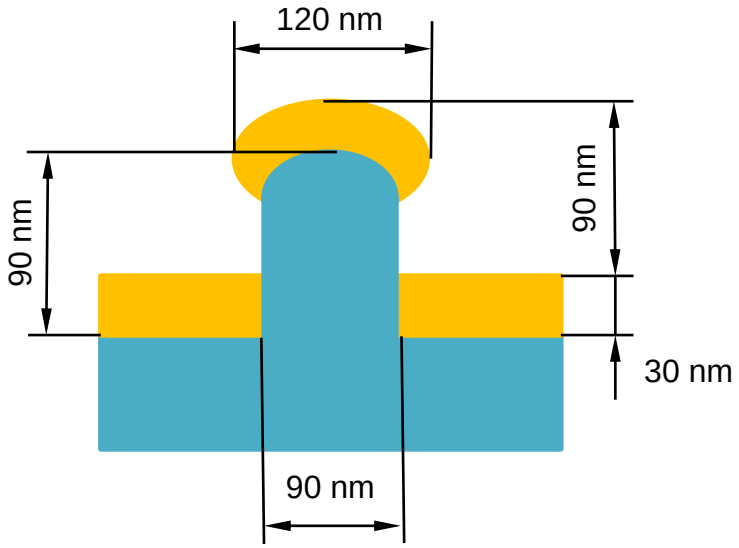

Fig. 32 Schematic model of the observed structure dimensions.

In order to validate the simulation approach, the experimentally observed structure was modeled with the geometry shown in Fig. 32 and the optical parameters were determined.

The reflectivity observed experimentally was in good agreement with the simulation results, as shown in Fig. 30b. Significant dampening is observed for the strongly coupled mode at ~760 nm, which is significantly broadened and slightly shifted towards shorter wavelength.

The near field distribution for the mushroom like structure, depicted in Fig. 33, suggests that the damped modes are localized in the gap between the metallic nanoparticle an the metallic layer. It is plausible that the metallic nanoparticles, which formed on the pillar walls, add significant dampening.

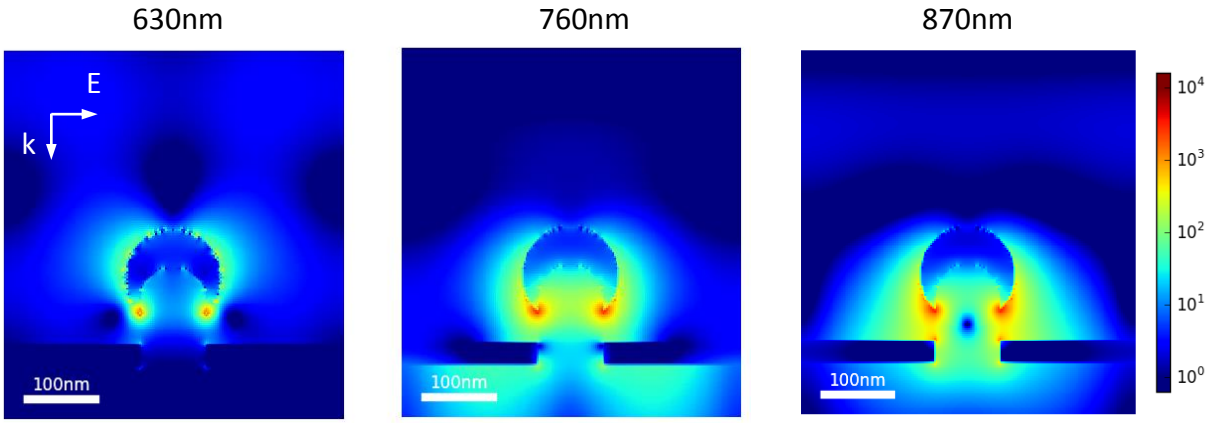

Fig. 33 E-field distribution for the experimentally observed nanostructure

7. Conclusion

This work presents highly tunable optically active nanostructures, which can be produced by nanoimprint lithography in combination with metal evaporation. As confirmed by AFM and SEM imaging, elevated nanoparticles formed on pillar tops are separated from a flat metal layer on the surrounding area. The resulting surface structure supports three resonant plasmonic modes in the optical wavelength range, whose resonant frequencies are tunable by geometric parameters with respect to their absolute position in the spectrum and also the relative position to each other. Computational studies of the optical near field further show a strong enhancement of the electrical field in the immediate vicinity of the nanoparticle surface, which can be utilized for plasmonic enhancement of fluorescence spectroscopy.

The method of UV-NIL was employed to prepare the polymer support structure. Further optimization of the procedure is needed in order to improve the pattern depth for high aspect ratio pillars. An important observation on all prepared samples was associated to the curvature of the imprinted pillar tops. This curvature affected the shape of the metallic nanoparticles and strongly influenced characteristics of supported surface localized plasmon modes. When taking into account this curvature in simulations, good agreement with experiments was achieved.

After fine tuning of the structures, the reported process holds potential for industrial upscaling to a roll-to-roll format with UV-NIL or hot-embossing structuring methods, which can be used for large scale manufacturing of plasmon enhanced fluorescence biosensor chips. The carried out simulations and experiments show that the prepared structure exhibit three plasmonic resonances that can be applied for probing of selective capture molecular analytes at the metallic nanoparticle walls or between the nanoparticle and underneath continuous metallic film.

The further optimization of the plasmonic structures, their interfacing with moieties for specific capture of target analytes in these areas and implementation to a plasmonically amplified fluorescence bioassay will be part of a follow up project.

8. Acknowledgements

I would like to thank:

First and foremost my group leader Dr. Jakub Dostalek at the Austrian Institute of Technology, who gave me the opportunity to work in the fascinating field of plasmonic biosensors.

Prof. DI Dr. Eisenmenger-Sittner for his kind offer to supervise my research from Vienna University of Technology.

Imran Khan for his support for my work on imprint lithography and optical spectroscopy.

Paul Müllner and Martin Bauch for providing access to a computational cluster and introduction to the field of simulations.

All my colleagues at AIT for sharing the ups and downs in research while still having an enjoyable time.

Last but not least, my family for their believe in me and their never-ending support.

9. Abbreviations

AFM	Atomic force microscopy
cLSP	Collective localized surface plasmon
FDTD	Finite difference time domain
FRET	Förster resonant energy transfer
EBL	Electron beam lithography
EF	Enhancement factor of fluorescence intensity
ELISA	Enzyme-linked immunosorbent assay
LIL	Laser interference lithography
LRSP	Long range surface plasmon mode
LOD	Level of detection
LSP	Localized surface plasmon resonance
NA	Numerical aperture
NIL	Nanoimprint lithography
QCMB	Quartz crystal microbalance
SEM	Scanning electron microscopy
SET	Surface energy transfer
SP	Surface plasmon
SPR	Surface plasmon resonance
T-NIL	Nanoimprint lithography using thermally cured polymers
UV	Ultraviolet
UV-NIL	Nanoimprint lithography using ultraviolet light cured polymers

10. List of symbols

α	polarizability
$\mathbf{B}$	magnetic flux density
β	surface plasmon wave vector component in propagation direction
c	speed of light
$\mathbf{D}$	dielectric displacement
e	charge of an electron
ε	permittivity
E	energy
$\mathbf{E}$	electric field
eV	electronvolt
h	Planck constant
$\mathbf{H}$	magnetic field
I	intensity
$\mathbf{J}$	current density
$\mathbf{k}$	wave vector
Λ	pattern or grating period
μ	permeability
$n(\omega)$	refractive index
$\mathbf{p}$	momentum
$\mathbf{P}$	polarization
ρ	charge density
σ	conductivity
σ^*	magnetic loss
ω	angular frequency
χ	electrical susceptibility

11. References

[1] H. Vaisocherová, H. Šípová, I. Víšová, M. Bocková, T. Špringer, M. Laura Ermini, X. Song, Z. Krejčík, L. Chrastinová, O. Pastva, K. Pimková, M. Dostálová Merkerová, J. E. Dyr, and J. Homola, “Rapid and sensitive detection of multiple microRNAs in cell lysate by low-fouling surface plasmon resonance biosensor,” *Biosens. Bioelectron.*, vol. 70, pp. 226–231, 2015.

[2] M. Bauch, S. Hageneder, and J. Dostalek, “Plasmonic amplification for bioassays with epi-fluorescence readout,” *Opt. Express*, vol. 22, no. 26, p. 32026, 2014.

[3] M. Bauch, “New enhancement strategies for plasmon-enhanced fluorescence biosensors,” 2014.

[4] N. Kooy, K. Mohamed, L. T. Pin, and O. S. Guan, “A review of roll-to-roll nanoimprint lithography.,” *Nanoscale Res. Lett.*, vol. 9, no. 1, p. 320, 2014.

[5] B. Sharma, R. R. Frontiera, A.-I. Henry, E. Ringe, and R. P. Van Duyne, “SERS: Materials, applications, and the future,” *Mater. Today*, vol. 15, no. 1–2, pp. 16–25, 2012.

[6] S. Lal, N. K. Grady, J. Kundu, C. S. Levin, J. B. Lassiter, and N. J. Halas, “Tailoring plasmonic substrates for surface enhanced spectroscopies,” *Chem. Soc. Rev.*, vol. 37, no. 5, p. 898, 2008.

[7] J. Dostálek and W. Knoll, “Biosensors based on surface plasmon-enhanced fluorescence spectroscopy.,” *Biointerphases*, vol. 3, no. 3, pp. FD12–D22, 2008.

[8] K. Kneipp, Y. Wang, H. Kneipp, L. T. Perelman, I. Itzkan, R. R. Dasari, and M. S. Feld, “Single Molecule Detection Using Surface-Enhanced Raman Scattering (SERS),” *Phys. Rev. Lett.*, vol. 78, no. 9, pp. 1667–1670, Mar. 1997.

[9] J. R. Lakowicz, Ed., *Principles of Fluorescence Spectroscopy*. Boston, MA: Springer US, 2006.

[10] P. R. Selvin, “The renaissance of fluorescence resonance energy transfer,” *America (NY).*, vol. 7, no. 9, 2000.

[11] C. S. Yun, A. Javier, T. Jennings, M. Fisher, S. Hira, S. Peterson, B. Hopkins, N. O. Reich, and G. F. Strouse, “Nanometal surface energy transfer in optical rulers, breaking the FRET barrier,” *J. Am. Chem. Soc.*, vol. 127, no. 9, pp. 3115–3119, 2005.

[12] D. Punj, M. Mivelle, S. B. Moparthi, T. S. van Zanten, H. Rigneault, N. F. van Hulst, M. F. García-Parajó, and J. Wenger, “A plasmonic ‘antenna-in-box’ platform for enhanced single-molecule analysis at micromolar concentrations,” *Nat. Nanotechnol.*, vol. 8, no. 7, pp. 512–516, 2013.

[13] S. A. Maier, *Plasmonics: Fundamentals and applications*. 2007.

[14] A. Taflove and S. C. Hagness, *Computational Electrodynamics: The Finite-Difference Time-Domain Method, Third Edition*. 2005.

[15] Kane Yee, “Numerical solution of initial boundary value problems involving maxwell’s equations in isotropic media,” *IEEE Trans. Antennas Propag.*, vol. 14, no. 3, pp. 302–307, May 1966.

[16] A. F. Oskooi, D. Roundy, M. Ibanescu, P. Bermel, J. D. Joannopoulos, and S. G. Johnson, “Meep: A flexible free-software package for electromagnetic simulations by the FDTD method,” *Comput. Phys. Commun.*, vol. 181, no. 3, pp. 687–702, 2010.

[17] M. Bauch and J. Dostalek, “Collective localized surface plasmons for high performance fluorescence biosensing,” *Opt. Express*, vol. 21, no. 17, pp. 637–644, 2013.

[18] S. Y. Chou, P. R. Krauss, and P. J. Renstrom, “Imprint Lithography with 25-Nanometer Resolution,” *Science (80-.).*, vol. 272, no. 5258, pp. 85–87, Apr. 1996.

[19] C. Peroz, S. Dhuey, M. Cornet, M. Vogler, D. Olynick, and S. Cabrini, “Single digit nanofabrication by step-and-repeat nanoimprint lithography,” *Nanotechnology*, vol. 23, no. 1, p. 015305, 2011.

[20] K. M. McPeak, S. V. Jayanti, S. J. P. Kress, S. Meyer, S. Iotti, A. Rossinelli, and D. J. Norris, “Plasmonic Films Can Easily Be Better: Rules and Recipes,” *ACS Photonics*, vol. 2, no. 3, pp. 326–333, 2015.

[21] H. Nakamura and I. Karube, “Current research activity in biosensors,” *Anal. Bioanal. Chem.*, vol. 377, no. 3, pp. 446–468, 2003.

[22] G. C. S. E. J. Zeman, “An Accurate Electromagnetic Theory Study of Surface Enhancement Factors for Ag, Au, Cu, Li, Na, Al, Ga, In, Zn, and Cd,” *J. Phys. Chem.*, vol. 91, no. 14, pp. 634–643, 1987.

[23] B. Ung, “The finite-difference time-domain method,” *Université Laval*, 2007. [Online]. Available: http://theses.ulaval.ca/archimede/fichiers/24879/ch02.html. [Accessed: 20-Oct-2015].

12. List of figures

13. List of tables